Quantifying spatiotemporal variability of ice algal blooms and the impact on surface albedo in southwest Greenland

Shujie Wang[1], Marco Tedesco[1,2], Patrick Alexander[1,2], Min Xu[3], Xavier Fettweis[4]

[1]Lamont-Doherty Earth Observatory, Columbia University, Palisades, NY 10964, USA.
5   [2]NASA Goddard Institute for Space Studies, New York, NY 10025, USA.
[3]Department of Geography, University of Alabama, Tuscaloosa, AL 35401, USA.
[4]Department of Geography, University of Liège, Liège 4000, BELGIUM

Correspondence to: Shujie Wang (swang@ldeo.columbia.edu)

10   **Abstract.** Albedo reduction due to light-absorbing impurities can substantially enhance ice sheet surface melt by increasing surface absorption of solar energy. Ice algae have been suggested to play a critical role in darkening the ablation zone in southwest Greenland. It was very recently found that the Sentinel-3 Ocean and Colour Instrument (OLCI) band ratio R_{709nm}/R_{673nm} can characterize the spatial patterns of ice algal blooms. However, Sentinel-3 was launched in 2016 and current data are only available over three melting seasons. Here, we demonstrate the capability of the MEdium Resolution Imaging 15   Spectrometer (MERIS) for mapping ice algae from space and extend the quantification of ice algal blooms over southwest Greenland back to the period 2004–2011. Several band ratio indices (MERIS chlorophyll indices and impurity index) were computed and compared with each other and against field measurements. The results indicate that the MERIS two-band ratio index (2BDA) R_{709nm}/R_{665nm} is very effective in capturing the spatial distribution and temporal dynamics of ice algal growth on bare ice in July and August. We analyzed the interannual (2004–2011) and summer (July–August) trends of algal abundance 20   and found significant increasing trends of ice algae close to the Jakobshavn Isbrae Glacier and along the middle dark zone between the altitudes of 1200 m and 1400 m. Using broadband albedo data from the Moderate Resolution Imaging Spectroradiometer (MODIS) we quantified the impact of ice algal growth on bare ice albedo, finding a 0.02~0.04 reduction rate in albedo for each algal population doubling. Our analysis indicates the strong potential for the satellite algal index to be used to reduce bare ice albedo biases in regional climate model simulations.

1 Introduction

Snow and ice play a critical role in regulating the global energy balance through high surface albedos (Skiles et al., 2018; Warren, 1982). The presence of light-absorbing impurities, including abiotic materials (such as mineral dust and black carbon; e.g. Flanner et al., 2007; Goelles and Bøggild, 2017; Wientjes et al., 2011) and biogenic materials primarily produced by microbial processes (Chandler et al., 2015; Ryan et al., 2018; Stibal et al., 2017; Williamson et al., 2019), can substantially 30   reduce the surface albedo of snow and ice and thus enhance surface melt. Increased meltwater further decreases surface albedo,

triggering a positive feedback mechanism between meltwater production and albedo decay (Box et al., 2012; Tedesco et al., 2011, 2016).

Snow algae and ice algae are among the main microbial communities in supraglacial environments, which are distributed in Greenland, Antarctica, Alaska, Svalbard, Himalaya, Siberia, the Rocky Mountains, and the European Alps (Anesio et al.,
35 2017). Algal growth on glaciers and ice sheets not only plays an important role in local and regional carbon and nutrient cycles but is also crucial for regulating surface melt processes through the reduction in snow and ice albedo resulting from dark algae pigmentation (Lutz et al., 2014; Remias et al., 2012; Stibal et al., 2017; Yallop et al., 2012). Snow algae (mainly Chlorophyceae) are psychrophiles residing in glacial snow or snowfield and bloom on snow surface after the onset of melting (Lutz et al., 2016, 2017). The visible colour of snow algae varies from green, to yellow to orange and red, and is determined
40 by the pigments (chlorophylls, xanthophylls, and secondary carotenoids, etc.) produced in different life stages. Ice algae (Zygnematales) are different from snow algae, and grow on the bare ice surface when liquid water, nutrients, and photosynthetically active radiation are sufficient (Lutz et al., 2018; Stibal et al., 2017; Yallop et al., 2012). The earliest documentation about ice algae dates to 1872. During an expedition to Greenland in 1870, Adolf Erik Nordenskiöld and fellow explorers found 'a brown polycellular alga' on ice surface and within cryoconite holes (Nordenskiöld, 1872). Several field
45 studies (Lutz et al., 2018; Stibal et al., 2015, 2017; Uetake et al., 2010; Yallop et al., 2012) have investigated the species composition and cell structures of ice algal communities. The primary ice algal species are Ancylonema nordenskiöldii, Mesotaenium berggrenii, and Cylindrocystis brebissonii, which are green microalgae and produce pigments including chlorophyll-a, chlorophyll-b, beta-carotene, lutein, and violaxanthin. Ancylonema nordenskiöldii and Mesotaenium berggrenii also generate a phenolic purpurogallin pigment (purpurogallin carboxylic acid-6-O-b-D-glucopyranoside) which absorbs
50 ultraviolet and visible radiation (Remias et al., 2012; Yallop et al., 2012). It has been suggested that this purpurogallin pigment accounts for the brownish-grey colour of the algae-laden ice (Tedstone et al., 2017).

Recent studies have revealed a significant impact of ice algal blooms on bare ice albedo in Greenland (Stibal et al., 2017; Williamson et al., 2018). Along the ablation zone over the southwest Greenland Ice Sheet, a dark ice band appears every summer season (Shimada et al., 2016; Tedstone et al., 2017). It was previously thought that this surface darkening was
55 primarily caused by outcropping of ancient dust (Wientjes and Oerlemans, 2010). Recently, widespread ice algal blooms were observed in the field and the dark pigments generated by ice algae were argued to be a primary control on the presence of the dark band (Ryan et al., 2018; Stibal et al., 2017; Williamson et al., 2018). Field sampling and spectral measurements indicate that ice algae have a greater effect on albedo reduction than other nonalgal impurities (Stibal et al., 2017). However, current field measurements of ice algal abundance and surface albedo are limited to a very few sites and melting seasons, and it is
60 logistically difficult to use the laboratory techniques to measure ice algae at a regional scale. The impact of ice algal development on surface albedo over large spatial and temporal scales has not yet been quantified.

Remote sensing provides a synoptic and efficient way to characterize geospatial phenomena across large spatial scales. To date, using remote sensing methods to quantify snow or ice algae extent or concentration is limited to a few studies (e.g. Ganey et al., 2017; Huovinen et al., 2018; Painter et al., 2001; Takeuchi et al., 2006; Wang et al., 2018). Painter et al. (2001) estimated

65 the algal abundance of the snow alga Chlamydomonas nivalis over a snow-covered region in the Sierra Nevada of California from the Airborne Visible/Infrared Imaging Spectrometer (AVIRIS) hyperspectral imagery based on chlorophyll absorption features between 630 nm and 700 nm. Despite the high capability of airborne hyperspectral imaging data for detecting chlorophyll, the availability of hyperspectral imaging data is constrained over space and time. Several studies (e.g. Takeuchi et al. 2006; Ganey et al. 2017; Huovinen et al. 2018) mapped red snow algae based on carotenoid absorption features using

70 satellite red and green bands. However, the use of carotenoid features in mapping ice algae is questionable, as ice algae do not, to our knowledge, generate secondary carotenoids like snow algae, and additionally, the spectral characteristics of dirt may resemble those of carotenoids (Painter et al., 2001; Takeuchi et al., 2006). While the brownish-grey colour of ice algae is attributed to the purpurogallin pigment, the detailed spectral and optical properties of purpurogallin are not well-understood, and the proper remote sensing bands/wavelength necessary to detect it are not yet known. Instead, chlorophyll-a, the primary

75 photosynthetic pigment, is generally used as a biomarker to detect algae from remote sensing data owing to its unique spectral signatures between 665-710 nm (Gitelson, 1992; Painter et al., 2001; Wang et al., 2018). The concentration of chlorophyll-a is commonly used as a proxy for algal biomass, upon which a number of algorithms have been developed to quantify the algal biomass in aquatic systems (Beck et al., 2016; Blondeau-Patissier et al., 2014; Matthews, 2011; Xu et al., 2019a, 2019b). Quantification of ice algae biomass from satellite data based on the chlorophyll-a feature has received less attention since the

80 chlorophyll-related satellite bands designed for land generally have coarse spectral resolutions.

Recently, Wang et al. (2018) demonstrated the capability of the Sentinel-3 Ocean and Land Colour Instrument (OLCI) in mapping ice algae based on the spectral signatures of chlorophyll-a at the red and near-infrared (NIR) spectrum range. OLCI is equipped with 21 spectral bands which include seven narrow chlorophyll-sensitive bands. OLCI's advanced band configuration makes it a valuable sensor for mapping algal blooms not only in water but also on ice. The spatial pattern of ice

85 algal abundance derived from the 709 nm to 673 nm OLCI reflectance ratio is consistent with field measurements collected on the southwest Greenland ice sheet (Wang et al., 2018). OLCI was designed based on the opto-mechanical and imaging design of MEdium Resolution Imaging Spectrometer (MERIS) onboard the European Space Agency (ESA)'s Envisat satellite, operational from March 2002 to April 2012, which collected data in 15 spectral bands between 390 nm and 1040 nm. MERIS data have been broadly used for atmospheric and oceanic studies, with the primary goal of measuring the concentration of

90 chlorophyll pigments and suspended sediments in oceans, coastal waters, and inland lakes (Gower et al., 2008; Palmer et al., 2015). MERIS features in particular a 709 nm band where high levels of chlorophyll-a have a characteristic reflectance peak. The similar configurations of the chlorophyll-targeted bands in terms of wavelength and bandwidth between MERIS and OLCI (Fig. 1a) point to the great potential of using MERIS data to reconstruct the spatial distribution of ice algae prior to 2012. In this study, we make use of the capability of MERIS for mapping ice algal blooms, extend the quantification of ice algae extent

95 and abundance in southwest Greenland back to 2004–2011, and further quantify the impact of ice algal blooms on bare ice albedo by combining the multiyear time series data of MERIS and MODIS.

2 Study area and data

2.1 Study area and previous field observations

Our study area is located between 66-71°N and 47-51°W in southwest Greenland. This area is featured by high ablation rates
100 and low surface albedos during summertime (Alexander et al., 2014; Fettweis et al., 2011; Moustafa et al., 2015; Stroeve et al., 2013). With the progression of surface melt over time, a dark ice zone forms rapidly and reaches a maximum area from mid-July to mid-August (Tedstone et al., 2017; Wang et al., 2018). The bare ice and dark ice areas are highly correlated to the meltwater production and surface runoff simulated by the regional climate model Modèle Atmosphérique Régionale (MAR) (Wang et al. 2018). The peaking time of surface darkening coincides with the occurrence of ice algal blooms observed in the
105 field. The ice alga Ancylonema nordenskiöldii and Mesotaenium berggrenii are the dominant species found in southwest Greenland during July and August (Lutz et al. 2018; Yallop et al. 2012; Williamson et al. 2018). Considering the growth season and surface habitat of ice algae, we focus our analysis on bare ice in July and August.

There are a limited number of field studies measuring ice algal abundance and reflectance spectra over our study area. Stibal et al. (2015) collected shallow surface ice cores and measured algal abundance over 14 sites in Greenland during May-
110 September 2013, in which the sites DS (69°28.56'N, 49°34.838'W), KAN_M (67°3.964'N, 48°49.356'W), and KAN_L (67°5.798'N, 49°56.303'W) are within our study area. KAN_M and KAN_L (Fig. 4a) are located along the Kangerlussuaq transect (K-transect), and DS (Fig. 4a) is located near to the Jakobshavn Isbrae Glacier. They documented the algal abundance (mean ± standard deviation values) averaged over the sampling period for each site. During the 2014 summer season, Stibal et al. (2017) collected both algal abundance and hyperspectral reflectance measurements via an Analytical Spectral Devices
115 (ASD) Field Spectrometer over a site near the automatic climate station S6 (67°04.779'N, 49°24.077'W) on the K-transect. They collected multiple samples each observation day and published the datasets of ice algal abundance and reflectance spectra at a 10 nm spectral resolution (Stibal et al., 2017). In this study, we used these field measurements both qualitatively and quantitatively as ground truth to validate the patterns of ice algal blooms derived from satellite data.

2.2 Satellite data

120 #### 2.2.1 MERIS Level-2 data

We used the full spatial resolution (300 m) MERIS Level-2 data acquired during July and August from 2004 to 2011 (https://earth.esa.int/web/guest/-/meris-full-resolution-full-swath-6015). The MERIS Level-2 data were processed from the Level-1b data (top-of-atmospheric radiances in 15 spectral bands shown in Fig. 1a). ESA adopted different processing techniques to generate the Level-2 data over land, water, and clouds. The Level-2 data over land include the normalized surface
125 reflectance in 13 spectral bands, corrected for the atmospheric effects of gaseous absorption and stratospheric aerosols (ESA, 2011). The full resolution Level-2 data from May 2002 to April 2012 were released at the MERCI file archive (https://merisfrs-merci-ds.eo.esa.int/) in February 2015. We identified 146 cloudless MERIS images acquired on 135 days from July to August between 2004 and 2011. Since there were no cloudless images available for the 2002 summer season and only three images

for the 2003 summer over the study area, we excluded these two years from our analysis. For those images affected by clouds
130 over the study area, we checked the MERIS Level-2 Flag data including the pixel types classified as water, land, and cloud. However, the Flag data fail to correctly capture all the cloud pixels due to algorithm limitations in differentiating clouds from other bright surfaces like snow and ice (ESA, 2011). In this regard, we manually removed the cloud pixels (patches) from each MERIS image.
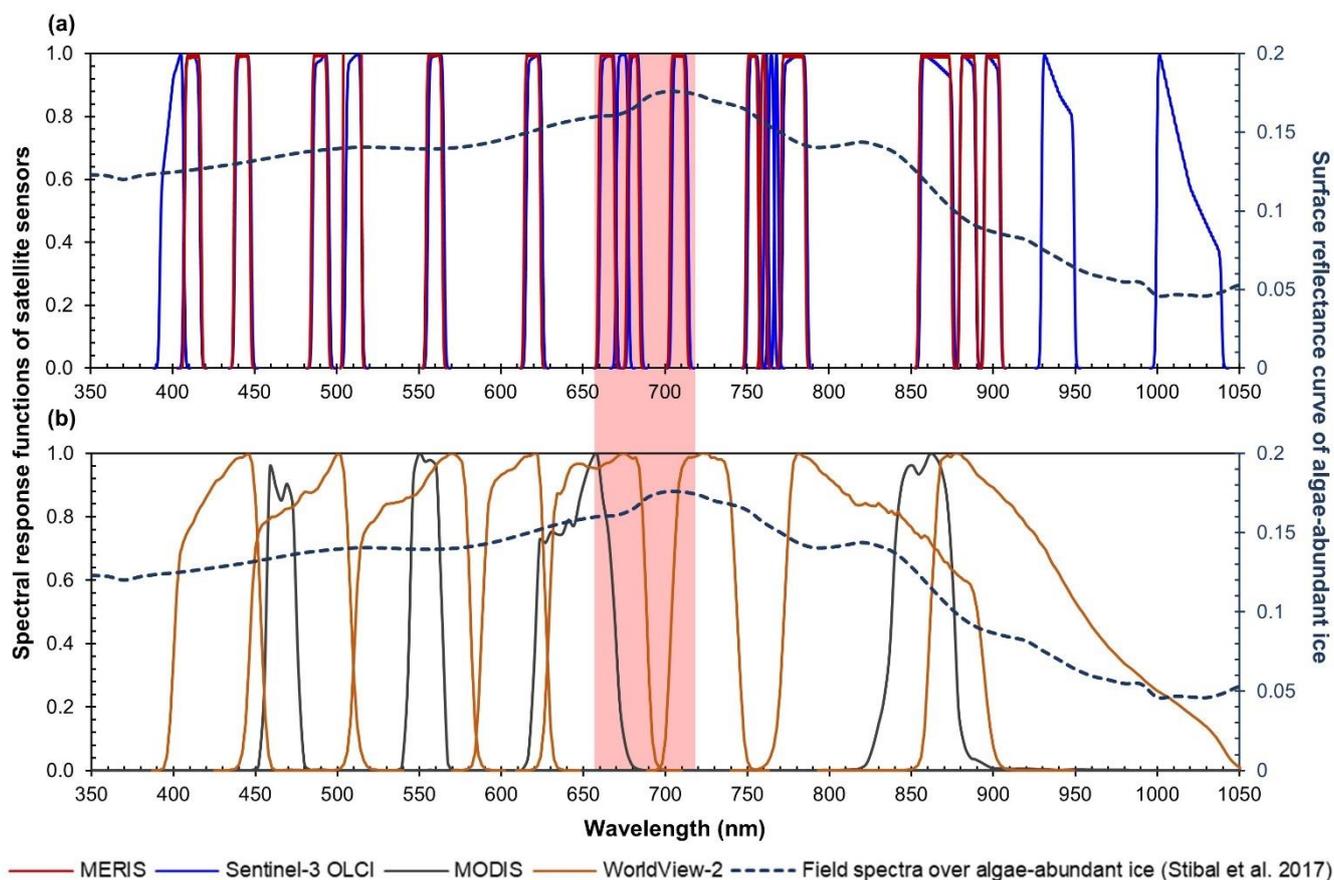
135 **Figure 1: Spectral response functions of (a) MERIS (red), OLCI (blue), and (b) MODIS (black), and WorldView-2 (orange) over the spectrum range of 350-1050 nm. All the MERIS and OLCI bands are within this range where photosynthetic and photoprotective pigments have spectral responses. Four MODIS bands (over land) and eight WorldView-2 bands are within this spectrum range, but with much coarser spectral resolutions. In both sub-plots, the dashed line shows hyperspectral ASD field spectroradiometer data (right vertical axis) collected over algae-abundant ice (Stibal et al., 2017), containing the chlorophyll-a signal at the red-NIR**
140 **wavelengths (red highlighted region).**

2.2.2 MODIS data

We used the MODIS/Terra daily surface reflectance product (MOD09GA Version 6) and daily snow cover product (MOD10A1 Version 6). The MOD09GA data include the atmospherically corrected surface reflectance at the MODIS bands of 620-670 nm, 841-876 nm, 459-479 nm, 545-565 nm, 1230-1250 nm, 1628-1652 nm, and 2105-2155 nm (Fig. 1b). The
145 MOD10A1 data include broadband albedo estimated based on the MOD09GA product. We used the version 6 data which are

greatly improved in sensor calibration, cloud detection, and aerosol retrieval and correction relative to version 5 (Casey et al., 2017; Lyapustin et al., 2014; Toller et al., 2013). Version 6 data are encouraged to be used for assessing temporal variability of surface albedo as they are corrected for sensor degradation issues impacting earlier versions (Casey et al., 2017). The spatial resolution of the MODIS datasets is 500 m. We resampled the MODIS data to 300 m using a nearest neighbour resampling
150   method. The cloud masks in the MOD10A1 data were applied to exclude the clouds.

2.2.3 WorldView-2 imagery

In addition to those previous field measurements, we also used WorldView-2 imagery to validate the spectral signal of ice algae on MERIS data. The WorldView-2 satellite was launched in October 2009, collecting data in nine spectral bands (titled panchromatic, coast, blue, green, yellow, red, red edge, NIR, and NIR2, Fig. 1b) at a very high spatial resolution (~2 m for the
155   multispectral bands). WorldView satellites have high geolocation accuracy owing to their three-axis stabilized platform equipped with high-precision GPS and attitude sensors (Wang et al., 2016). Although the WorldView-2 spectral bands have wide bandwidths, the red (630-690 nm) and red edge (705-745 nm) bands can capture the chlorophyll-a signal (Fig. 1b), which have been used for mapping algal species in nearshore marine habitats (Reshitnyk et al., 2014). We obtained WorldView-2 imagery acquired in July and August (2009-2011) from the Polar Geospatial Center (PGC, https://www.pgc.umn.edu/). The
160   images were provided as orthorectified top-of-atmospheric radiances in eight multispectral bands. We performed atmospheric corrections to the radiance images and obtained surface reflectance images using the MODerate resolution atmospheric TRANsmission (MODTRAN) based Fast Line-of-sight Atmospheric Analysis of Hypercubes (FLAASH) (Anderson et al., 2002). The sub-Arctic model and rural aerosol model were used for correction of atmospheric effects caused by water vapour and aerosols (Legleiter et al., 2013).

2.3 Modèle Atmosphérique Régionale (MAR) outputs

The regional climate model Modèle Atmosphérique Régionale (MAR, Fettweis et al., 2017) combines atmospheric modelling (Gallée and Schayes, 1994) with the Soil Ice Snow Vegetation Atmosphere Transfer Scheme (De Ridder and Gallée, 1998) to simulate surface energy balance and mass balance processes over the Greenland and Antarctic ice sheets. In this study, we examined the relationship between the MAR albedo bias (e.g. Alexander et al., 2014; Moustafa et al., 2015) and ice algal
170   blooms. The snow albedo in MAR is determined by snowpack temperature, temperature gradient, and liquid water content, and the bare ice albedo is scaled based on the accumulated surface water (Alexander et al., 2014). Since the MAR albedo scheme does not account for impurities, there are significant biases between the MAR albedo and MODIS albedo over the southwest Greenland ablation zone (Alexander et al., 2014). We used the 7.5 km resolution MAR v3.9 daily outputs, forced by the European Centre for Medium-Range Weather Forecasts Interim Reanalysis (ERA-Interim; Dee et al., 2011). MAR v3.9
175   features minor bug fixes and differences in tuning relative to MAR v3.5.2 (Fettweis et al., 2017).

3 Methods

3.1 Bare ice mapping

We mapped bare ice cover from each MERIS image using a thresholding method applied to surface reflectance data (e.g. Shimada et al., 2016; Tedstone et al., 2017; Wang et al., 2018). To be consistent with previous studies, we used MODIS-
180 derived bare ice maps as reference to determine the optimal threshold for the MERIS data. We removed tundra and ocean pixels using the MEaSUREs Greenland Ice Mapping Project classification mask (Howat et al., 2014). We selected 31 MOD09GA images that were coincident with MERIS overpasses and were cloud free over the study area. Following Tedstone et al. (2017), we applied a threshold to the 841-876 nm reflectance ($R_{841-876\ nm}$), using the criterion $R_{841-876\ nm}<0.6$ to extract bare ice reference maps from selected MODIS images. For coincident MERIS images, we iteratively applied a threshold value
185 ranging from 0 to 1, increasing by 0.01 at each iteration to the MERIS band 13 (865 nm) and compared MERIS and MODIS bare ice cover. The optimal threshold was determined based on the F1 score accuracy metric which is the harmonic average of precision and recall, defined as following:

$$F1 = 2 * (precision * recall) / (precision + recall) \tag{1}$$

190

where *precision* is calculated using $N_{TP} / (N_{TP} + N_{FP})$ and *recall* is calculated using $N_{TP} / (N_{TP} + N_{FN})$. N_{TP} is the number of true positives (the number of pixels classified as bare ice by both the MODIS and MERIS data), N_{FP} is the number of false positives (the number of pixels that are only classified as bare ice by the MERIS data), and N_{FN} is the number of false negatives (the number of pixels that are only classified as bare ice by the MODIS data). Average F1 score was calculated for each threshold
195 based on those 31 image pairs. The threshold of 0.53 yielded the highest F1 score (0.957). We also excluded supraglacial lakes using the modified normalized difference water index (MNDWI, Yang and Smith, 2013), defined as:

$$MNDWI = (R_{blue} - R_{red}) / (R_{blue} - R_{red}) \tag{2}$$

200 where R_{blue} is the reflectance at 442 nm (MERIS band 2) and R_{red} is the reflectance at 665 nm (MERIS band 7). Pixels with MNDWI greater than 0.14 (Yang and Smith, 2013) were identified as lake pixels and excluded from analysis. Using the same iterative method described above, we also determined an optimal threshold of 0.47 to extract dark ice pixels (pixels with bare ice containing substantial surface impurities) using the 620 nm band, following Shimada et al. (2016) and Tedstone et al. (2017). This band was commonly used to delineate dark ice by applying a threshold based on the assumption that visible
205 wavelengths including the red band are mostly affected by light-absorbing impurities rather than surface water and grain size variations (Tedstone et al., 2017).

3.2 Ice algae mapping from MERIS spectra ratio indices

Chlorophyll-a is the primary photosynthetic pigment generated by ice algal cells (Williamson et al., 2018; Yallop et al., 2012). Hyperspectral field measurements (Cook et al., 2019; Stibal et al., 2017) and the Sentinel-3 OLCI spectra (Wang et al., 2018)

210 both show the typical spectral signatures of chlorophyll-a at the red and NIR wavelengths over the algae-abundant ice surface, featured by a reflectance peak around 709 nm and absorption features around 665-681 nm. Pure ice, in contrast, has increased absorption at 709 nm as compared to shorter wavelengths (Hall and Martinec, 1985). The magnitude of the reflectance peak at 709 nm relative to 665-681 nm is highly dependent on the chlorophyll-a content (Binding et al., 2013; Gitelson, 1992). Figure 2d shows the MERIS spectra over a dark ice pixel, compared with the WorldView-2 spectra and the field hyperspectral

215 measurements by Stibal et al. (2017). The selected MERIS pixel, located near to the Jakobshavn Isbrae Glacier, is close to the site DS where Stibal et al. (2015) measured a high abundance of ice algae during the 2013 summer season. The MERIS image (Fig. 2a) was acquired on 5 July 2010, and the WorldView-2 image (Fig. 2b and Fig. 2c) was acquired on 9 July 2010. Despite the differences in absolute values of surface reflectance, the spectral shapes of the MERIS, WorldView-2 and field spectra match quite well, particularly with regard to the presence of the chlorophyll-a spectral signal, which validates the ice algal

220 signal in the MERIS data.
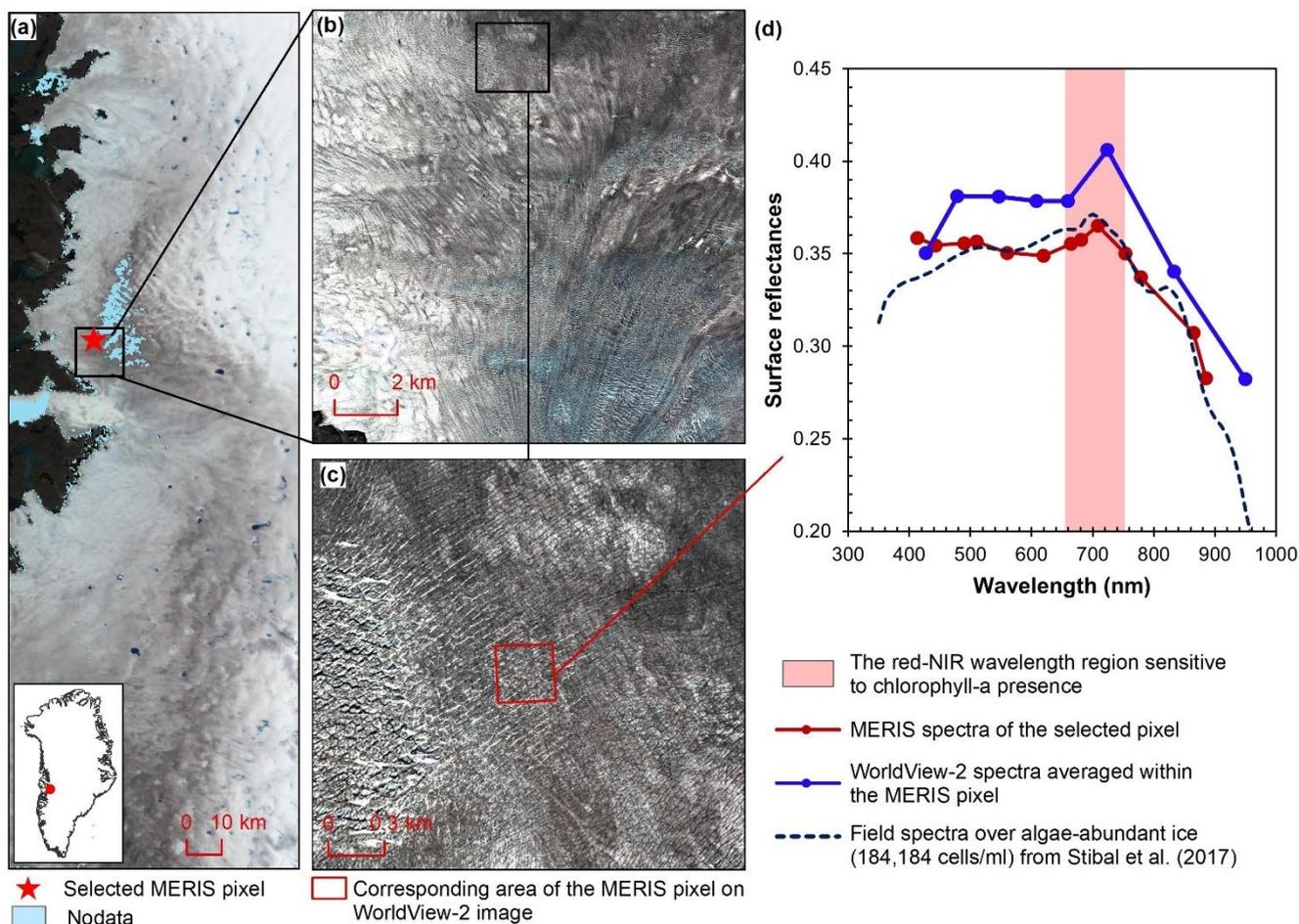
Figure 2: Comparison between the MERIS, WorldView-2, and field spectra over algae-abundant dark ice. (a) MERIS Level-2 image (true colour composite) acquired on 5 July 2010. Pixels with missing data are shown in blue. (b) WorldView-2 surface reflectance image acquired on 9 July 2010 over the square area in (a). (c) Zoomed-in WorldView-2 image, with the area (red square) corresponding to the selected MERIS pixel in (a). (d) Reflectance spectra comparison between MERIS, WorldView-2, and the field hyperspectral measurements collected over the algae-abundant ice at S6 by Stibal et al. (2017).

In order to identify the best means of quantifying ice algae, we calculated a number of different band ratio indices (Table 1), including the well-established MERIS chlorophyll indices (Moses et al., 2012; Mishra and Mishra, 2012; Binding et al., 2013) and the Impurity index (Dumont et al., 2014). The two-band (2BDA) and three-band (3BDA) red-NIR algorithms have been widely applied to estimation of chlorophyll-a concentration in aquatic systems (Beck et al., 2016; Moses et al., 2009; Xu et al., 2019a, 2019b), and proved to be highly accurate to retrieve chlorophyll-a content in turbid waters with complex optical properties from MERIS data (Moses et al., 2012). The normalized difference chlorophyll index (NDCI, Mishra and Mishra, 2012) was defined following the concept of the normalized difference vegetation index (NDVI). The maximum chlorophyll index (MCI) measures the height of the 709 nm reflectance peak relative to the baseline interpolated by the reflectances at 681 nm and 753 nm (Binding et al., 2013). The Impurity index is different from the chlorophyll indices mentioned above, as it

does not utilize the chlorophyll-a spectral characteristics. This index was constructed to quantify the snow impurity content over Greenland Ice Sheet (Dumont et al., 2014) based on the assumption that impurities decrease the reflectance at visible bands more than the NIR bands.

240 **Table 1. Details on the different ratio indices.**

Indices	Equation	MERIS bands
Two-band NIR–Red index (2BDA)	R_{709nm} / R_{665nm}	B7, B9
Three-band NIR–Red index (3BDA)	$(R_{665nm}^{-1} - R_{709nm}^{-1}) / R_{753nm}$	B7, B9, B10
Normalized Difference Chlorophyll Index (NDCI)	$(R_{709nm} - R_{665nm}) / (R_{709nm} + R_{665nm})$	B7, B9
Maximum Chlorophyll Index (MCI)	$(R_{709nm} - R_{681nm}) - (R_{753nm} - R_{681nm}) * (709 - 681) / (753 - 681)$	B8, B9, B10
Impurity index	$\ln(R_{560nm}) / \ln(R_{865nm})$	B5, B13

4 Results

4.1 Comparison between different ratio indices

Figure 3 shows the MERIS spectra over four distinct sites. Each site represents a typical surface type such as clean bare ice, dark ice with a significant chlorophyll signal, dark ice with a less significant chlorophyll signal, or a supraglacial lake. Figure

245 3b shows that each surface type is characterized by a distinct spectral curve, particularly between the two dark sites. Both of these sites have a surface reflectance at 620 nm of less than 0.47 and are classified as 'dark ice' based on the thresholding method discussed above (Shimada et al., 2016; Tedstone et al., 2017). The difference is that the northern dark ice site has a chlorophyll spectral signature between 665 nm and 753 nm that matches the field spectra of algae-abundant ice (Fig. 2d), while at the southern dark ice site, the reflectance peak at 709 nm is much less pronounced. We calculated the ratio indices including

250 2BDA, 3BDA, NDCI, MCI, and Impurity index over bare ice ($R_{865 nm}<0.53$) for each MERIS image. The chlorophyll indices of 2BDA, 3BDA, and NDCI use similar spectral bands and are in general very highly correlated to each other. Table 2 lists the ratio indices and the surface reflectance at 620 nm over those four sites based on the MERIS image acquired on 14 August 2011. It is shown that the chlorophyll indices of 2BDA, 3BDA, and NDCI are highest over the northern dark ice site where we identified the chlorophyll signal, and lowest over the supraglacial lake. In contrast, the chlorophyll index of MCI cannot

255 well represent the chlorophyll signal we observed, which reaches a maximum over the clean bare ice. This may be due to the fact that MCI is more suitable for monitoring intense algal blooms with very high chlorophyll concentrations in water (Binding et al. 2013) while not applicable to the ice algal blooms with comparatively lower chlorophyll content. In addition, MCI measures the height of the 709 nm reflectance peak relative to the baseline between 681 nm and 753 nm, which could be also sensitive to the bare ice spectrum. Therefore, we selected the 2BDA index to characterize the ice algal abundance owing to its

260 simplicity and effectivity. For the Impurity index, the clean bare ice has the lowest value, followed by the supraglacial lake, dark ice with the weaker chlorophyll signal, and dark ice with the stronger chlorophyll signal. Table 2 shows that the

supraglacial lake also has a high Impurity index relative to clean ice, suggesting that the Impurity index may include the darkening effect caused by meltwater presence.
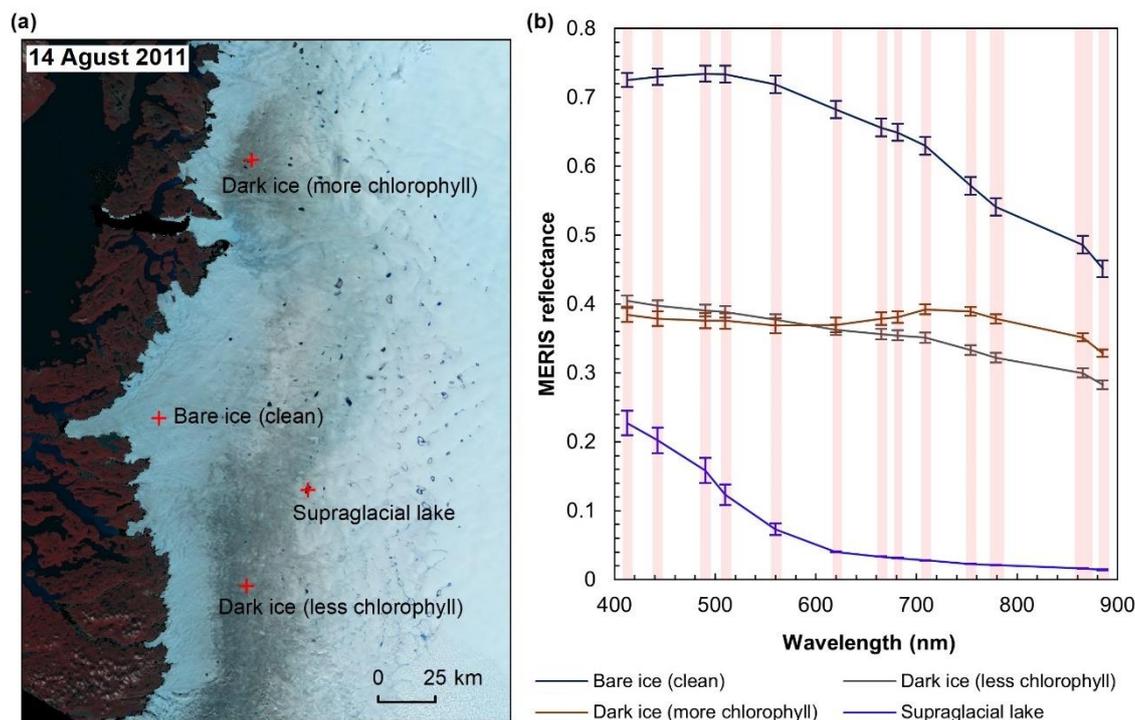
Figure 3: MERIS spectra of different surface types. (a) MERIS Level-2 image (false colour composite) acquired on 14 August 2011 and locations of the four different sample sites. Each site has an area of 1.2 km by 1.2 km, composed of 16 MERIS pixels. (b) MERIS surface reflectance in 13 spectral bands over the four sites, illustrated by the mean and standard deviation values for each band over each site.

Table 2. The calculated ratio indices and the surface reflectance at 620 nm over the four sites.

Surface type	2BDA	3BDA	NDCI	MCI	Impurity	R_{620nm}
Bare ice (clean)	0.960	-0.112	-0.021	0.011	0.457	0.683
Dark ice (more chlorophyll)	1.035	0.231	0.017	0.008	0.955	0.369
Dark ice (less chlorophyll)	0.986	-0.122	-0.007	0.005	0.809	0.362
Supraglacial lake	0.839	-250.106	-0.087	0.000	0.635	0.040

Figure 4 shows the spatial patterns of the mean 2BDA index, Impurity index, surface reflectance at 620 nm, and MODIS broadband albedo for the bare ice zone, averaged over those MERIS images acquired on 135 days from 2004 to 2011. Figure 4a suggests ice algae are abundant at the DS region close to the Jakobshavn Isbrae Glacier between the altitudes of 600 m and 1200 m, and in the middle ablation area (68.5°N-66.5°N) between 1200 m and 1400 m, these patterns are consistent with those of ice algal maps derived from the Sentinel-3 OLCI data for the 2016 and 2017 summer season (Wang et al., 2018). The

relative magnitude of the 2BDA values between the DS, KAN_L, and KAN_M sites also matches the field measurements of ice algal abundance (Stibal et al., 2015). Figure 4b indicates that the spatial extent of the high Impurity index region in the middle ablation area extends lower in elevation than the area of high algal index (1000 m to 1400 m for the Impurity index vs.

280 1200 m to 1400 m for the algae index). The Impurity index was designed to capture all types of impurities, indicating the presence of both abiotic (e.g. outcropping particulates; Wientjes et al., 2012) and biological impurities, which is incapable of distinguishing ice algae from other impurities. A map of surface reflectance at 620 nm (Fig. 4c) was generated for comparison with the algal and impurity index maps, since this band was commonly used to delineate dark ice by applying a threshold (determined to be 0.47 for the MERIS data). Similar to the Impurity index, the dark ice area ($R_{620\ nm}$<0.47) is not only limited

285 to the algae-abundant areas. Compared with the elevation level of 1200 m – 1400 m, the zone between 1000 m and 1200 m has lower surface reflectance at 620 nm (Fig. 4c) as well as lower MODIS broadband albedo (Fig. 4d). Comparison between these four maps suggests that highly-abundant ice algae were present at the DS area and the middle 1200 m – 1400 m area, while the darkening at the middle 1000 m – 1200 m area could be attributed to longer exposure of bare ice and increased consolidation of particulates with melt (Tedesco et al., 2016), where the 'wavy' patterns caused by ancient dust outcropping

290 were also observed (e.g. Wientjes and Oerlemans, 2010).
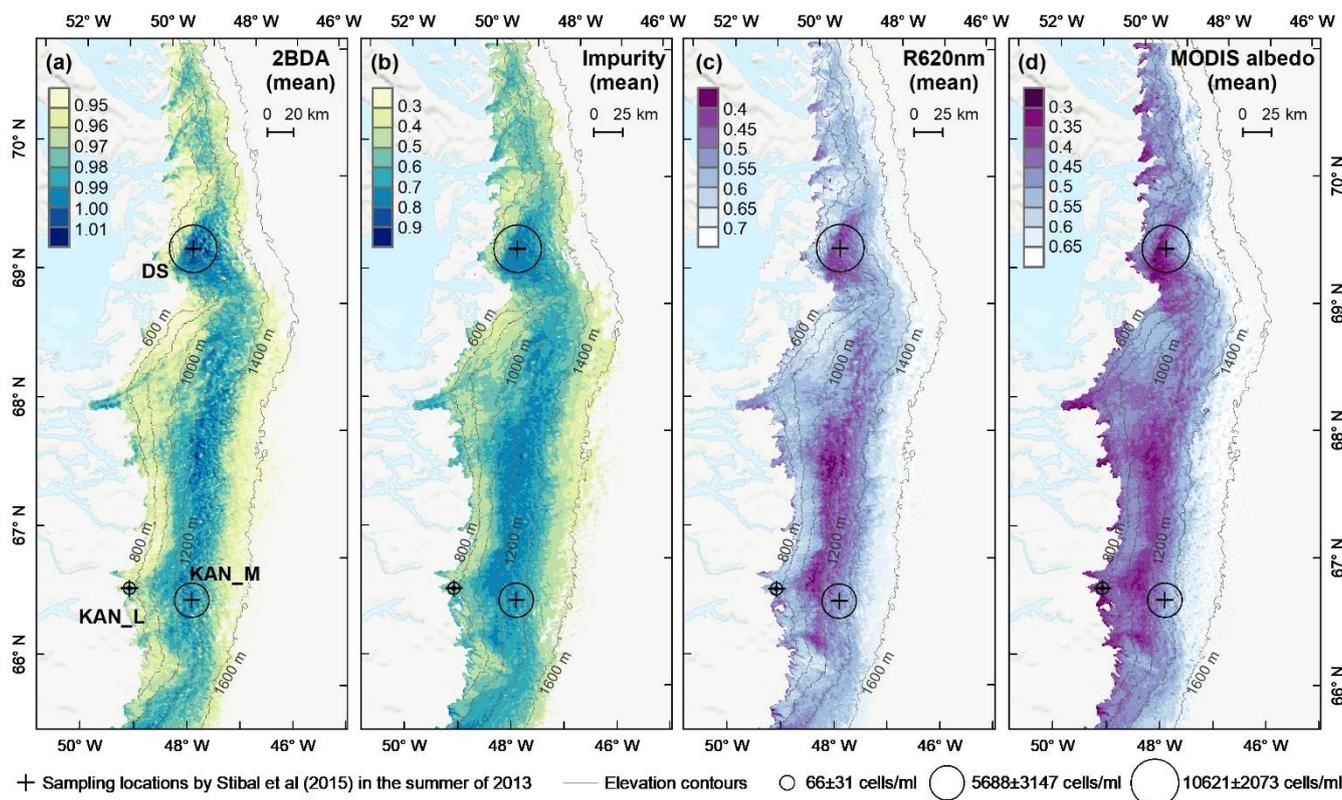
Figure 4: Spatial patterns of the mean 2BDA index (a), Impurity index (b), surface reflectance at 620 nm (c), and MODIS broadband albedo (d) over the bare ice zone during July and August from 2004 to 2011. The elevation contours illustrate the spatial variations

of each variable with altitude. The cross labels show the spatial locations of the field sites DS, KAN_L, and KAN_M measured by
295 Stibal et al. (2015), along with the magnitude (circle labels) of ice algal abundance for each site.

4.2 Interannual trends of ice algal blooms, impurity content, and surface albedo

The annual time series (July-August mean) of the 2BDA index (Fig. 5a) and the Impurity index (Fig. 5b) show the interannual
variability of algal abundance and impurity content, indicating a general increasing trend of bare ice area, algal abundance,
and total impurity content from 2004 to 2011, particularly after 2006. The spatial extent of ice algae expanded towards higher
300 elevations (1200 m – 1400 m). Between 2004 and 2011, the 2BDA index reached a maximum in 2010 when high air
temperatures and intensive surface melt occurred over Greenland (Tedesco et al., 2011). The Impurity index has similar
interannual variability to the 2BDA index, but exhibits different spatiotemporal variations between 1000 m – 1200 m and 1200
m – 1400 m at the middle ablation area. The interannual variability of the 2BDA and Impurity indices is also coherent with
variability in Greenland ice sheet-wide summer albedo, which was lowest in 2010 and highest in 2006 for the period 2004 –
305 2011 (Tedesco et al., 2018).
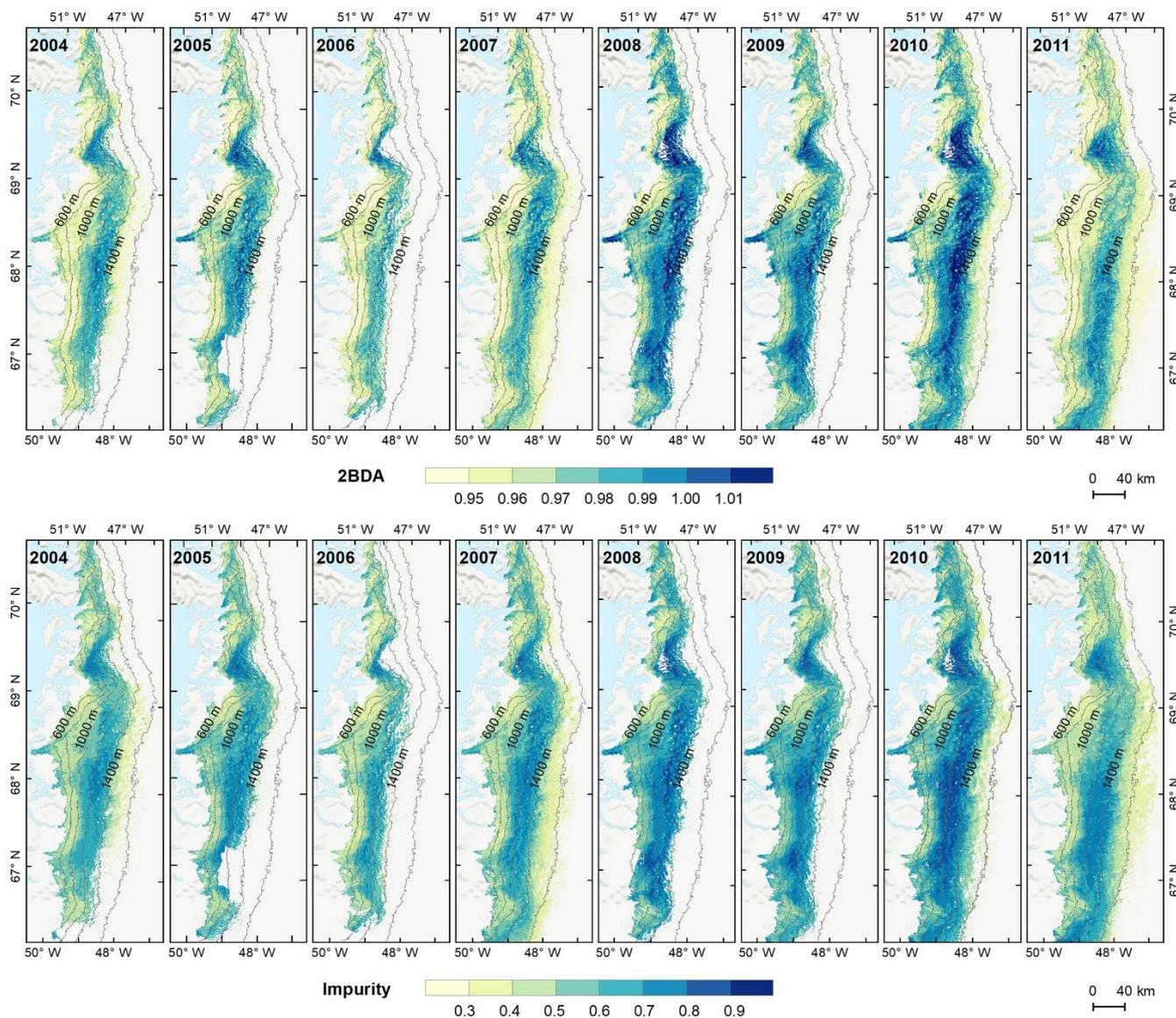
Figure 5: Maps of mean 2BDA index (a) and Impurity index (b) over July and August from 2004 to 2011.

We calculated the interannual trends of the 2BDA index, Impurity index, and MODIS broadband albedo using linear regression analysis, with the mean 2BDA index, Impurity index or MODIS albedo for each year as the dependent variable and the year

310   as the independent variable. Pixels with observations during fewer than five years were discarded from the analysis. Figure 6 shows the regression coefficients for 2BDA, Impurity, and MODIS albedo vs. time, and the corresponding R^2 estimates are shown in Fig. A1. There were two primary regions (Fig. 6a) that had significant increases in algal abundance from 2004 to 2011, including the DS region in the north and the southern region between 68.5°N and 66.5°N between 1200 m and 1400 m in elevation. The interannual trend of the Impurity index (Fig. 6b) shows larger spatial extent with significant increasing trend

315   as compared with the 2BDA index. Figure 6c shows that the areas with increasing algal abundance and increasing impurity index also had significant albedo (July-August mean) reduction from 2004 to 2011. The albedo reduction was 0.025~0.04 per year over the K-transect area (between 1200 m and 1400m in elevation) and the DS area. The spatial patterns of declining albedo more closely match the patterns of impurity index as opposed to the 2BDA index, suggesting that the impurity index quantifies multiple processes related to surface darkening in addition to ice algae cover.
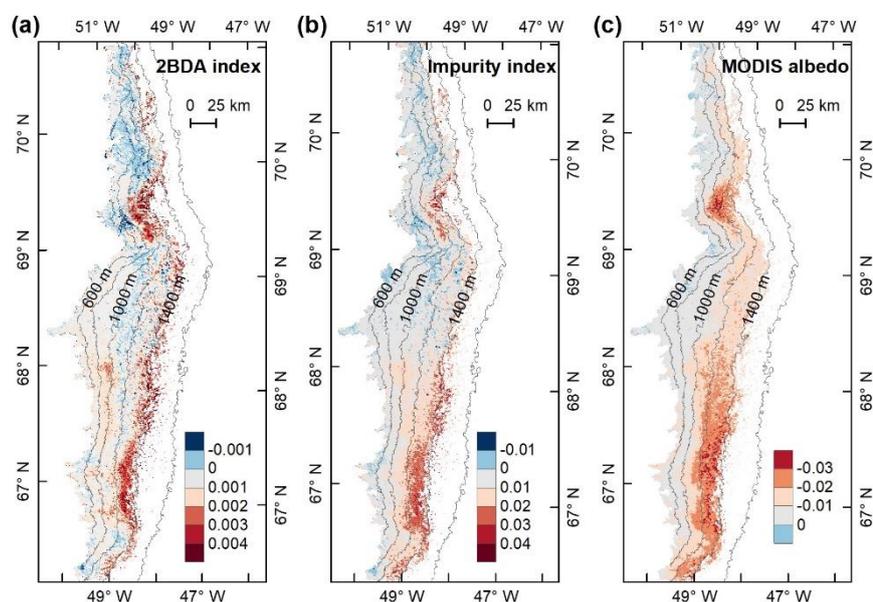
320

Figure 6: Interannual trends (regression coefficients with year) of the 2BDA index (a), Impurity index (b), and MODIS albedo (c) from 2004 to 2011.

4.3 Ice algal development over summer months of July and August

To better understand seasonal dynamics of ice algae, we examined intra-annual trends in the 2BDA index during the months

325   of July and August. We estimated the temporal trend of the 2BDA index from July to August for each MERIS pixel. For each pixel and each day, we calculated the average 2BDA index using the same day 2BDA indices of multiple years. To account for the differences between different years, we applied a temporal smoothing function with a window size of three days to the daily average 2BDA data. Pixels with more than 15 days of observations were kept for linear regression analysis, with the daily 2BDA index as dependent variable and the time (day) as independent variable. Our results indicate that the 2BDA index

330   can also capture the temporal dynamics of ice algal development during summer. Figure 7 shows a comparison between the time series of the 2BDA index and the field measurements of ice algal abundance over the K-transect observation site (S6) at 67° 04.779' N, 49° 24.077' W (Stibal et al., 2017). The field measurements were collected during the 2014 summer season. We calculated the mean algal abundance for each observation day and converted it to cell doubling scale using the logarithmic function. The daily 2BDA index (left axis in Fig. 7) was calculated by aggregating the same day 2BDA indices of multiple

335   years between 2004 and 2011. It is shown that 2BDA index has coherent temporal trends with the field measurements,

particularly the increasing trend from mid-July to mid-August. This time window is consistent with rapid algal colonization observed in field (Stibal et al., 2017; Williamson et al., 2018; Yallop et al., 2012; Lutz et al. 2018). A similar mid-July to mid-August increase was also found by Wang et al. (2018) using Sentinel-3 OLCI data.
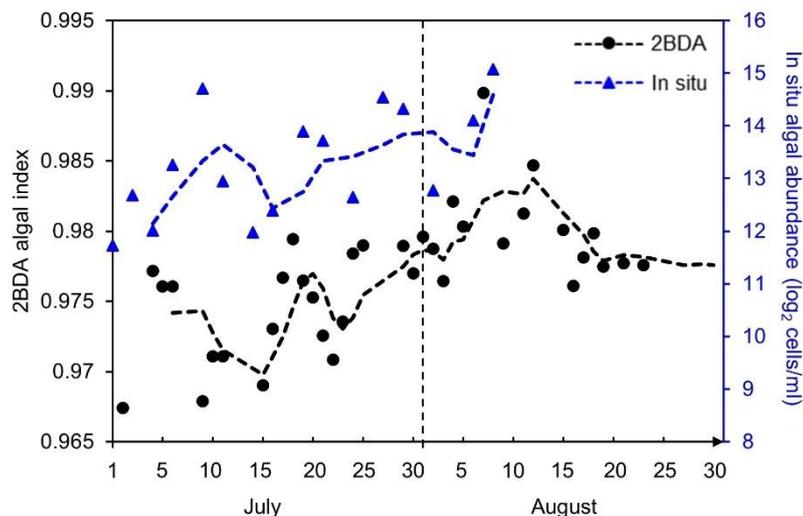
Figure 7: The July-August time series of the 2BDA index (2004-2011) and the field measurements of ice algal abundance (2014) at the Stibal et al. (2017) field site S6.

Figure 8a shows the daily 2BDA time series at the three field sites KAN_L, KAN_M, and DS, as examples of areas with different seasonal trend patterns, while Figs. 8b and c show the spatial distribution of seasonal trends across the west coast ablation area. The three field sites illustrate the temporal evolution of algal abundance. There was no significant temporal trend in 2BDA index at KAN_L, and the 2BDA index was less than 0.98 through July and August. In comparison, the 2BDA index at KAN_M and DS had statistically significant increasing trends with time, and the 2BDA values were mostly greater than 0.98, indicating that dramatic algal growth occurred at KAN_M and DS through the summer season. This pattern is highly consistent with the measured ice algal abundance during the 2013 summer (Stibal et al., 2015). The site KAN_L had fewer ice algal cells (66±31 cells/ml) than the sites KAN_M (5688±3147 cells/ml) and DS (10621±2073 cells/ml), and ice algal blooms appeared to be more intense at DS than KAN_M. The time series in Fig. 8a suggest that the period of algal growth at the KAN_M occurred primarily between mid-July and mid-August, with the start of growth occurring later than at the DS site. Between 20 July and 20 August, the regression coefficient was 0.0009 day^{-1} for both DS and KAN_M, suggesting a nearly constant growth rate during the fast proliferation stage of ice algae. Throughout July and August, the regression coefficient was 0.0007 and 0.0004 for DS and KAN_M, respectively. To test whether this period of algal growth was consistent, across the region, we calculated temporal trends for 20 July–20 August (Fig. 8c). The magnitude of trends is larger for this period and R^2 values are higher over a broader region, suggesting that this shorter period of growth occurs over a wide region. In the DS region, however, the R^2 values and magnitude of trends are similar for the two periods, indicating that the growth period is longer in the DS region relative to other areas (consistent with the KAN_M vs. DS time series).
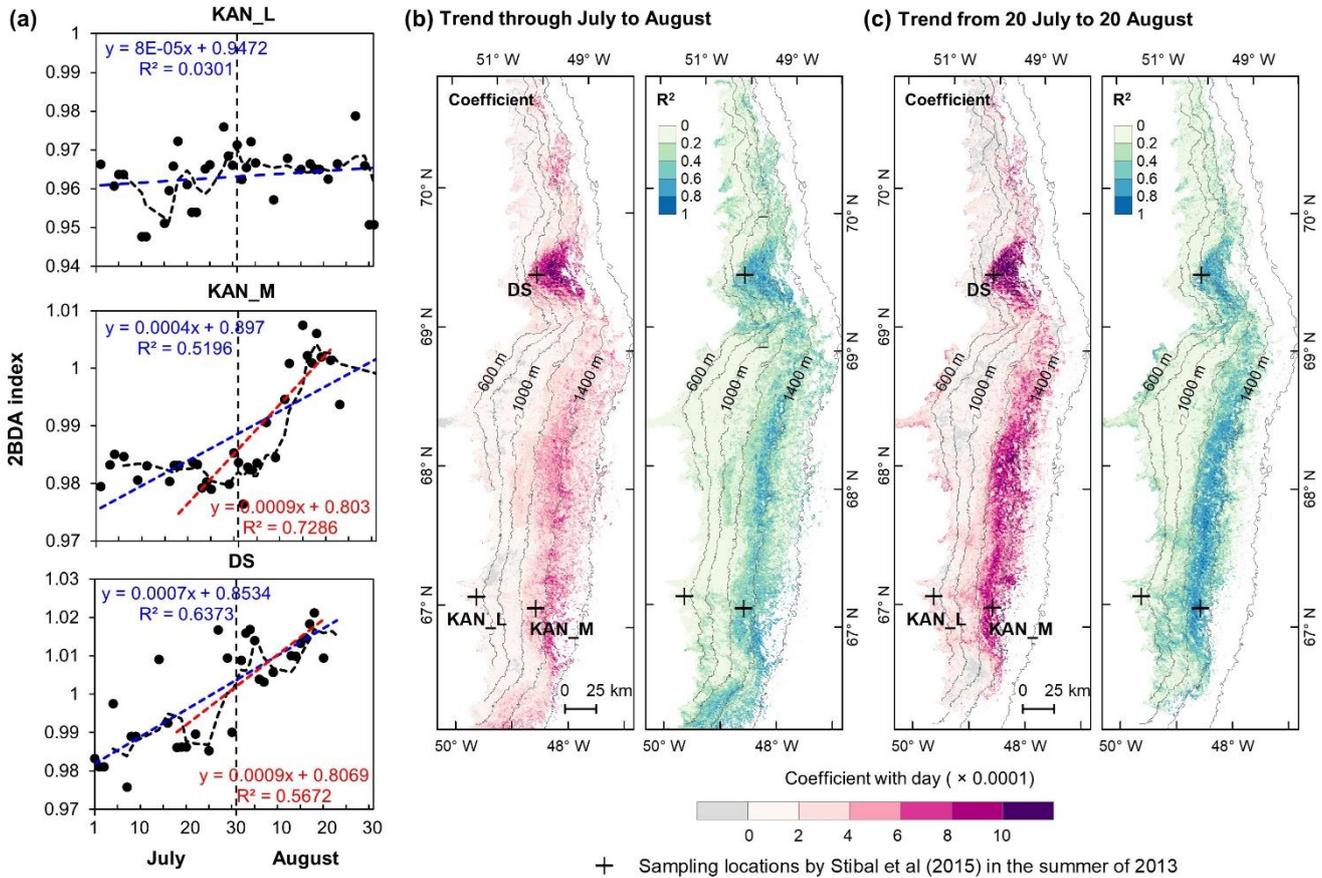
Figure 8: Temporal trends of the 2BDA index over July and August. (a) 2BDA time series and temporal trend analysis over KAN_L, KAN_M, and DS. (b) Regression coefficients and R² estimates of the temporal trend analysis for the period of July–August. (c) Regression coefficients and R² estimates of the temporal trend analysis for the period of 20 July–20 August.

To make our estimates more comparable to previous studies, we calculated the algal population doubling time for the different regression coefficients of the 2BDA index with time. Wang et al. (2018) derived an empirical relationship between the Sentinel-3 OLCI reflectance ratio R_{709nm}/R_{673nm} and the ice algal abundance, represented as

$$y=10^{-35} e^{87.015x} \tag{3}$$

where x denotes the reflectance ratio and y denotes the algal abundance (cells/ml). Given the similarity between the OLCI and MERIS band configurations and the negligible differences between the 673 nm and 665 nm reflectance, we used Eq. (3) to derive the relationship between the MERIS 2BDA index (x) and algal population doubling ($\log_2 y$ cells/ml) as

$$\log_2 y = \log_2 e * 87.015 * x - 35 * \log_2 10 \tag{4}$$

Therefore, based on the regression coefficient (denoted as a) of 2BDA versus time, the algal population doubling time can be approximated as $1 / (\log_2 e * 87.015 * a)$, as listed in Table 3. The areas with significant algal growth trend ($R^2 > 0.5$) between 20 July and 20 August (Fig. 8c) had a mean regression coefficient of 0.00076±0.0002, and a mean algal population doubling

time of 11.2±2.6 days. The DS area had faster algal growth rate than other areas, which was estimated to be 9.6±2.7 days. This

375 estimate is comparable to the field study by Williamson et al. (2018) who reported a doubling time of 7.18±1.04 days for algae-

abundant ice (K-transect).

Table 3. Algal population doubling time for different regression coefficients of 2BDA index with day

Regression coefficient	Population doubling time (days)
0.0004	19.91
0.0005	15.93
0.0006	13.28
0.0007	11.38
0.0008	9.96
0.0009	8.85
0.001	7.97

4.4 Impact of ice algal blooms on surface albedo in July and August

380 We quantified the impact of ice algal blooms on surface albedo in July and August based on the daily time series data of the

2BDA index and MODIS broadband albedo. Similar to deriving the July-August trend of 2BDA index, we generated a daily

albedo time series after averaging and smoothing the MODIS daily albedo data from 2004 to 2011. Figure 9 shows the derived

temporal trends of MODIS albedo from 1 July to 20 August. The days after 20 August were excluded from analysis since

snowfalls often happened in late August. The DS area had the most significant albedo reduction over July and August, up to

385 0.4~0.6% per day. In the middle ablation zone between the altitudes of 1000 m and 1200 m the albedo reduction rate was

0.2~0.4% per day, and the reduction rate was 0.2~0.3% per day in the zone between 1200 m and 1400 m in elevation.
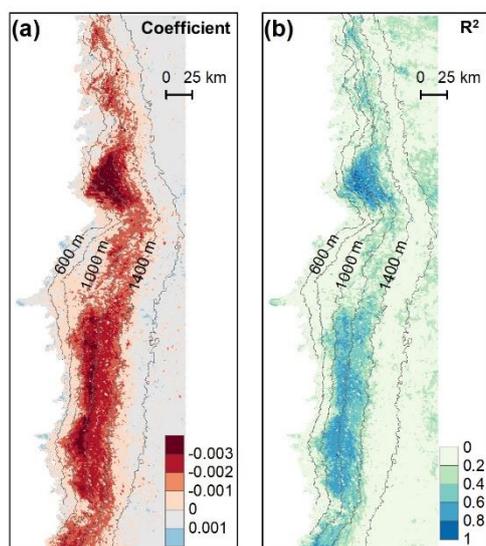
Figure 9: Temporal trends of MODIS albedo in July and August. (a) Regression coefficients of surface albedo with time (day) from 1 July to 20 August. (b) Corresponding R² estimates.

390   We converted the 2BDA index (x) to algal population doubling (log₂y) using the derived Eq. (4) in section 4.3. Figure 10 shows results of a regression analysis for algal population doubling vs. surface albedo. The analysis shows a statistically significant correlation between algal growth and albedo reduction at the DS area between the altitudes of 800 m and 1200 m, the middle ablation zone between the altitudes of 1200 m and 1400 m, and the 1000–1200 m area nearby the K-transect. Over these areas, the regression coefficient ranged between -0.04 to -0.02, indicating a surface albedo decrease of 2~4% for each

395   algal population doubling. This estimate is comparable to results from the field study by Stibal et al. (2017) who estimated a net albedo reduction of 0.038±0.0035 for each algal population doubling based on the in-situ measurements of ice algal abundance and coincident surface albedo. In general, ice algal growth explains most of the temporal variability of surface albedo in July and August, except the middle area between 1000 m and 1200 m in elevation where there are probably other factors contributing to the observed albedo reduction.
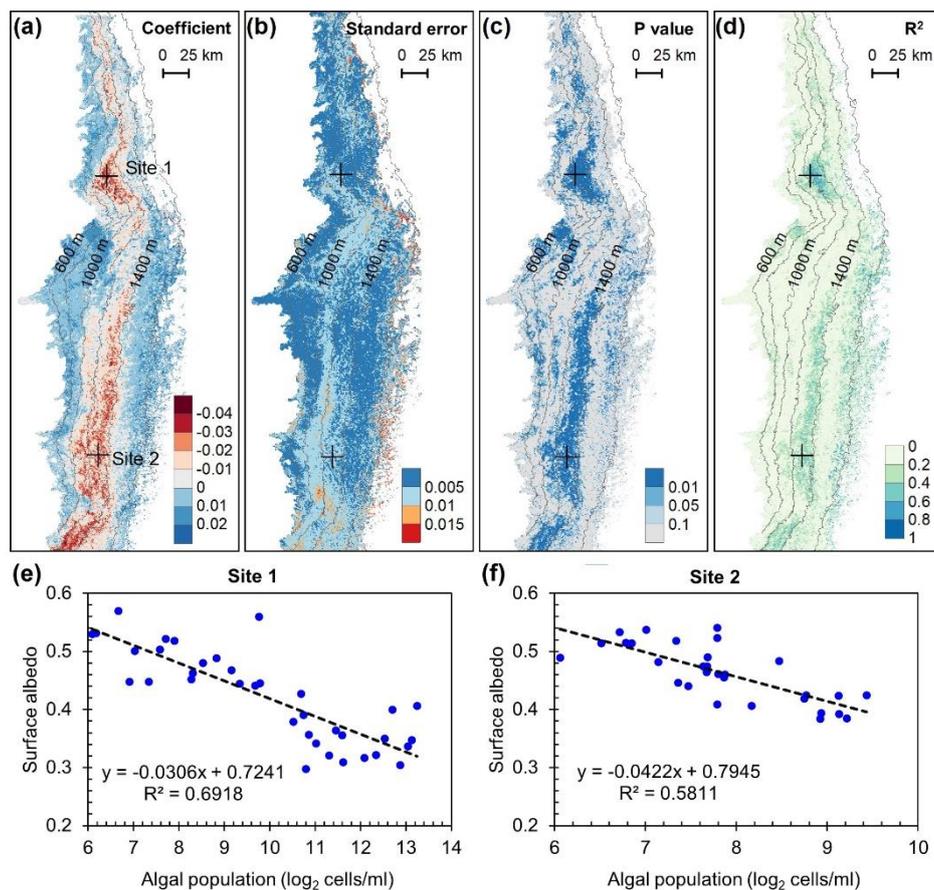
400

Figure 10: Relationship between algal population and surface albedo. (a) Regression coefficients. (b) Standard errors of the correlation coefficients. (c) P values. (d) R² values. (e) and (f) show algal population versus surface albedo at Site 1 and Site 2, respectively.

5 Discussion

405 In this study, we demonstrated that MERIS data can be used for characterization of the spatial distribution and temporal dynamics of ice algal blooms in southwest Greenland. This enables the construction of a long-term time series data of ice algae in combination with the new-generation satellite sensor Sentinel-3 OLCI in the future. Despite the moderate spatial resolution of the MERIS sensor, its narrow bandwidths and specific band wavelengths designed for chlorophyll make the MERIS archive data a powerful tool to study the spatiotemporal variability of algal communities in supraglacial environment. The chlorophyll

410 signal of ice algae presented in the MERIS spectra is very consistent with the coincident (nearly) WorldView-2 data and the field hyperspectral measurements collected over algae-abundant ice. Similar to the Sentinel-3 OLCI ratio index R_{709nm}/R_{673nm}, the MERIS 2BDA index R_{709nm}/R_{665nm} can effectively quantify the algal growth pattern through July to August. This ratio index is further supported by a very recent study (Cook et al., 2019) which shows that the ratio of the reflectance peak at 709 nm relative to 665 nm increases with ice algal abundance based on the field measurements of algal abundance and coincident

415 reflectance spectra.

Our analysis indicates that surface albedo decreases by 0.02~0.04 for each algal population doubling during July and August primarily in algae-abundant areas close to the Jakobshavn Isbrae Glacier and within the middle ablation zone (68.5°N-66.5°N) between 1200 m and 1400 m in elevation. It is also important to know whether the MERIS 2BDA index could explain the discrepancy between the satellite albedo and climate model albedo, which is fundamental to improve the albedo scheme and

420 surface energy budget estimates in regional climate models like MAR. Previous studies (e.g. Alexander et al., 2014) have demonstrated a positive albedo bias of MAR in comparison with the MODIS albedo along the southwest Greenland Ice Sheet, which results from the fact that the algae and other impurities are not yet included in the albedo scheme. Figure 11a shows the comparison between MODIS albedo and MAR albedo over the study area (including both bare ice and snow), indicating the overestimation of MAR albedo for the dark areas with MODIS albedo less than 0.5. There was a significant negative correlation

425 between the albedo difference (MODIS albedo minus MAR albedo) and the 2BDA index (Fig. 11b), which means that the positive MAR albedo bias increases with the algal abundance.
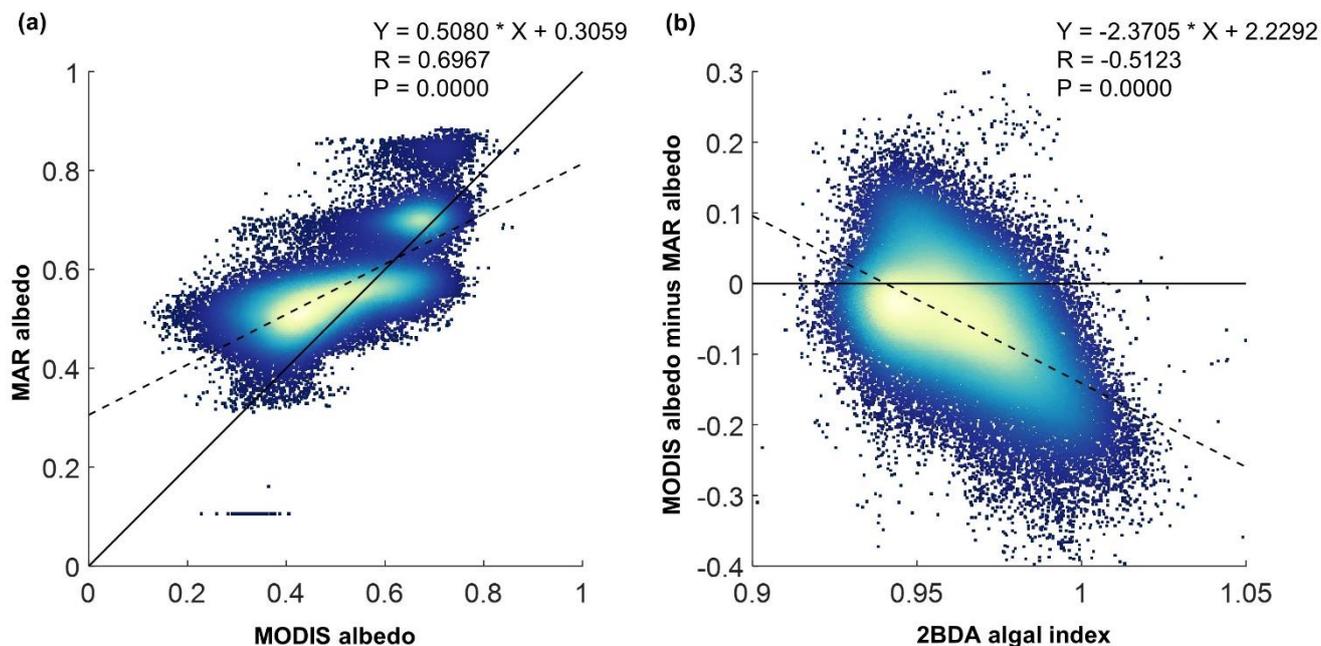
Figure 11: (a) Comparison between MAR albedo and MODIS albedo over the study area for July and August from 2004 to 2011. The dashed line and equation show the linear fitting between MODIS albedo and MAR albedo. The black line is the 1:1 reference line. (b) Relationship between the MERIS 2BDA index and the albedo difference between MODIS and MAR. The colour scheme in both (a) and (b) illustrates the data distribution density (yellow means higher density, and blue means lower density).

The spatial pattern of the albedo bias (Fig. 12a) is consistent with the impurity distribution. Over the dark areas, the MAR albedo was overestimated by 0.16±0.03 as compared to the MODIS albedo. We further examined the relationship between the albedo bias (MODIS albedo minus MAR albedo) and the algal population, finding a significant correlation between them in the DS area (Fig. 12b and Fig. 12c). Figure 12d indicates that each population doubling can explain -0.0274 bias between the MODIS and MAR albedos. Although there are also negative correlations between the algal population and the MODIS-MAR albedo difference like Fig. 12d at the middle zone between 1000 m and 1400 m, the correlations are less significant as compared to the DS area. This is consistent with our previous analysis that the albedo reduction at 1000 m – 1200 m is poorly related to algal growth. In addition to parameterizing the ice algal growth, other processes related to albedo reduction caused by impurities such as consolidation of impurities melted from snow should be also accounted in the future.
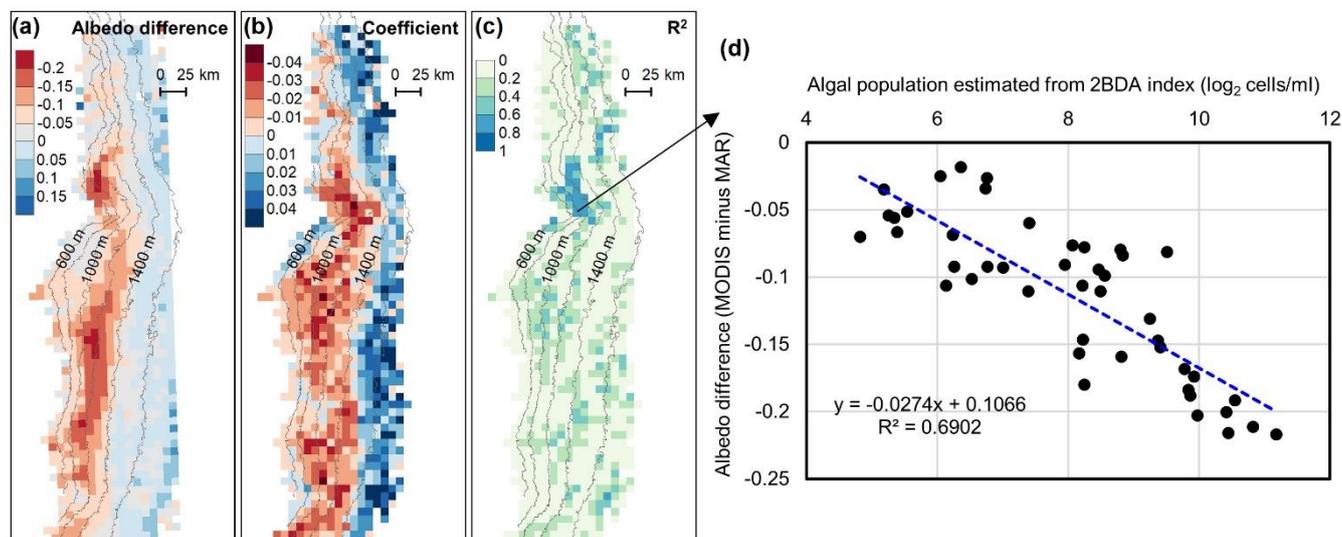
Figure 12: (a) Albedo difference between MODIS albedo and MAR albedo (MODIS albedo minus MAR albedo) averaged over the study period. (b) Regression coefficients of albedo difference with 2BDA-derived algal population (log₂ cells/ml). (c) R² estimates for the regression analysis. (d) Scatterplot of albedo difference versus algal population doubling over the DS algae-abundant area and the linear fitting equation.

Due to the increasing trend of ice algal blooms and their significant impact on bare ice albedo, it is fundamental to understand the factors affecting the algal growth. Lutz et al. (2018) analysed the composition of ice algal communities near the K-transect between 27 July and 14 August 2016 using high-throughput sequencing and subsequent oligotyping techniques. The ice algae species of Ancylonema nordenskiöldii and Mesotaenium berggrenii were found as the dominant taxa. Ice algae lack a flagellated stage and are less capable of migrating upwards to snow layers at the beginning of melting season (Anesio et al., 2017). Therefore, the ice algal growth is restricted to bare ice surface, which is consistent with our finding that ice algal blooms tend to occur extensively from late-July to mid-August when the bare ice is mostly exposed and less affected by snowfalls. The areas at lower altitude have longer duration of bare ice exposure, whereas intense ice algal blooms occur at higher altitude up to 1200 m – 1400 m along the middle ablation zone. The growth of ice algae also depends on the availability of liquid water and nutrients in addition to the surface habitat of bare ice. Particulates melted from ancient ice layers have been suggested to be an important nutrient source for ice algae growth (Stibal et al., 2017; Wientjes et al., 2012). Although liquid water is a prerequisite for algal growth, Wang et al. (2018) found a negative correlation between algal abundance and meltwater production, which was attributed to hydrological flushing of algae during periods of excessive meltwater and surface runoff (Takeuchi, 2001; Uetake et al., 2010). Figure 13a-b show the relationships between the 2BDA index and the topographic variables as well as the near surface temperature and meltwater production simulated by MAR. For each two variables, we separated the data into two-dimensional bins and calculated the average 2BDA index for each bin. It is suggested that ice algae are mostly distributed over flat areas with less topographic undulations (Fig. 13a). The areas suitable for ice algal growth have moderate but not excessive melting conditions (Fig. 13b). This further supports the hypothesis that active hydrological

processes have a negative effect on algal development. In regard to the suitable temperature, ice algae are so far known to be
465   well adapted to the temperature close to the freezing point of water (Anesio et al., 2017). Although no significant correlations
have been found between algal abundance and air temperature, the algal growth appears to be affected by cold freezing
temperatures as suggested by Fig. B1 which shows the daily simulated near surface temperature along with the in situ measured
algal abundance (Stibal et al. 2017) at the K-transect S6 station in 2014 summer. Figure 13c-e show the MAR-simulated
shortwave and longwave downward radiation fluxes, cloud cover, snowfall, rainfall, meltwater production, and near surface
470   temperature averaged over July and August across the study area from 2004 to 2011. The high 2BDA algal index in 2008-
2010 (Fig. 5a) coincides with less cloud cover and more incoming shortwave radiation (Fig. 13c). This period is also
characterized by less rainfalls (Fig. 13d), reducing the hydro-flushing possibility. Figure 13e shows that the years of 2008 and
2009 with high algal index had less melting and lower temperature than the other years, suggesting that meltwater production
and air temperature play a less dominant role than shortwave radiation in ice algal development. Given the importance of
475   shortwave radiation for photosynthesis of ice algae, we argue that air temperature, surface melt, and bare ice exposure are
important factors at the beginning stage of ice algal habitat development, while downward shortwave radiation has a primary
control on the proliferation stage of ice algae. These dynamics may relate to the atmospheric circulation change in Greenland,
with patterns of anomalous anticyclonic circulation and higher 500 hPa geopotential height becoming more frequent (e.g.
Hanna et al., 2016; Mioduszewski et al., 2016), associated with reduced cloud cover (Hofer et al., 2016) and increased
480   downward shortwave radiation. Therefore, it is vital to understand the interactions between the supraglacial microbiome and
climate change (Cavicchioli et al., 2019) for better projection of future ice sheet mass balance.
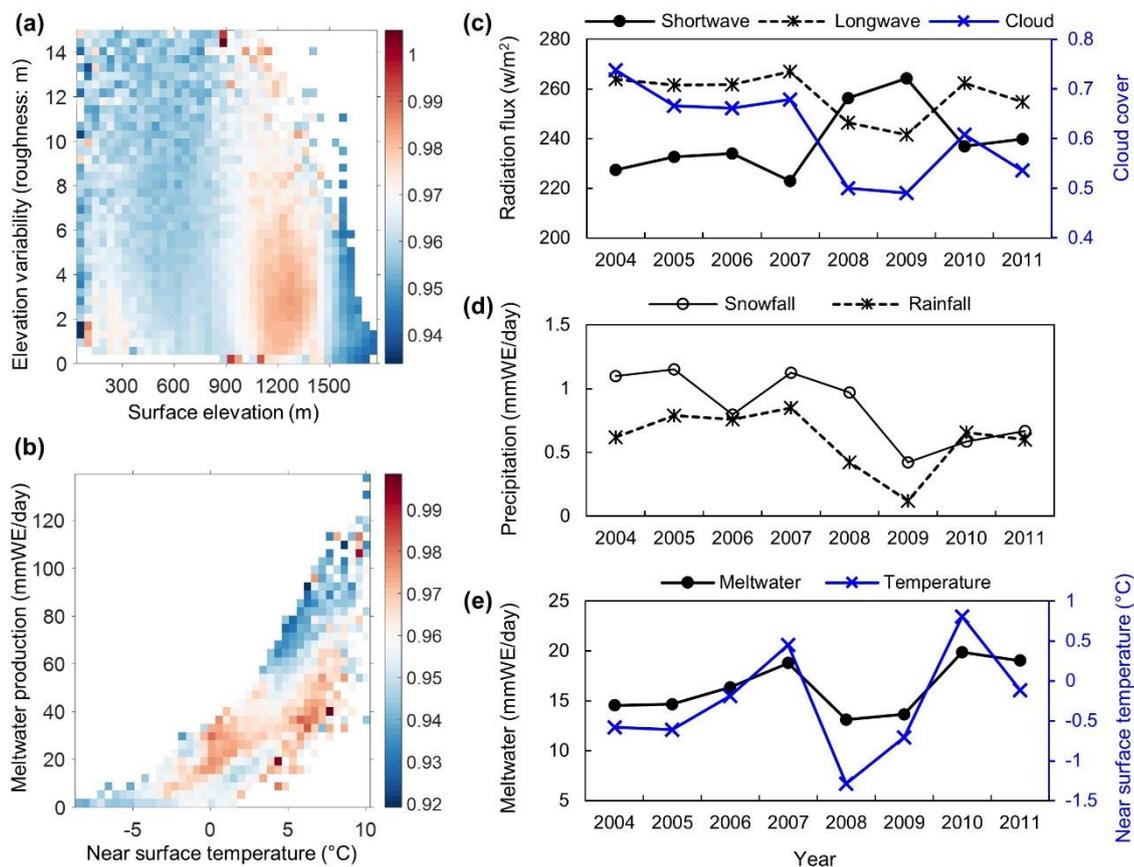
Figure 13: (a) 2BDA index versus surface elevation and roughness (elevation variability within each MERIS pixel). (b) 2BDA index versus near surface temperature and meltwater production simulated by MAR. The colour bars in (a) and (b) indicate the average 2BDA index for each two-dimensional bin defined by the two variables on horizontal and vertical axis. (c) July-August mean of downward shortwave and longwave radiation fluxes and cloud cover over the study area from 2004 to 2011. (d) July-August mean of rainfall and snowfall. (e) July-August mean of meltwater production and near surface temperature.

485

6 Conclusions

We examined the spatiotemporal variability of ice algal blooms in southwest Greenland during July and August from 2004 to

490   2011 using the chlorophyll detection capability of MERIS. We calculated a number of remote sensing ratio indices including

chlorophyll indices and impurity index. The results indicate that similar to the Sentinel-3 OLCI ratio index of R_{709nm}/R_{673nm},

the MERIS 2BDA index of R_{709nm}/R_{665nm} can effectively quantify the spatial distribution and seasonal growth pattern of ice

algae, with results highly consistent with field measurements. There was an increasing trend of ice algal abundance and

impurity content at the dark area close to Jakobshavn Isbrae Glacier and the area close to K-transect at altitude of 1200 m –

495   1400 m, being coherent with the reducing trend of surface albedo in this period. We quantified the impact of ice algal growth

on surface albedo over July and August, and found that each algal population doubling would decrease the surface albedo by

2~4 percent. Our analysis points to the great potential of using the satellite ratio index to parameterize the impact of ice algae on surface albedo and thereby reducing the albedo bias in regional climate models. Nevertheless, the surface darkening along the middle ablation zone between 1000 m and 1200 m in elevation cannot be well explained by algal growth, indicating that

500 other processes related to surface darkening need further investigation and quantification. Future research should also be directed toward understanding the climate drivers of ice algae variability and parameterizing their growing dynamics using regional climate model outputs.

Data availability

The MERIS level-2 data are available at the MERCI file archive (https://merisfrs-merci-ds.eo.esa.int/), courtesy of the

505 European Space Agency. The MODIS MOD09GA and MOD10A1 data can be accessed from the NASA Land Processes Distributed Active Archive Center (https://search.earthdata.nasa.gov/). The WorldView-2 imagery were provided by the Polar Geospatial Center (PGC, https://www.pgc.umn.edu/) at the University of Minnesota. MAR v3.9.3 outputs are available at ftp://ftp.climato.be/fettweis/.MARv3.9.3.

Appendix A

510
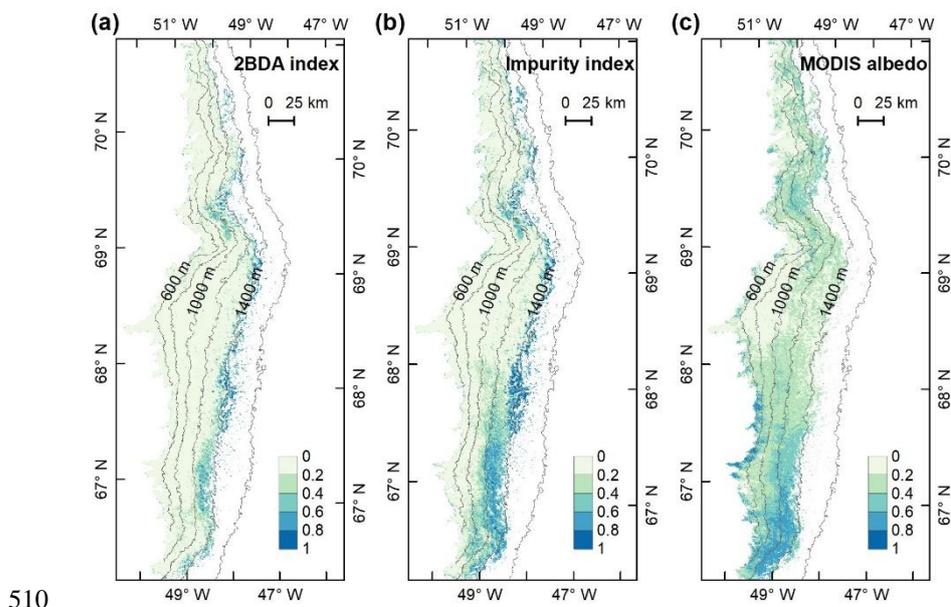
Figure A1. R^2 of interannual trends of the 2BDA index (a), Impurity index (b), and MODIS albedo (c) from 2004 to 2011.

Appendix B
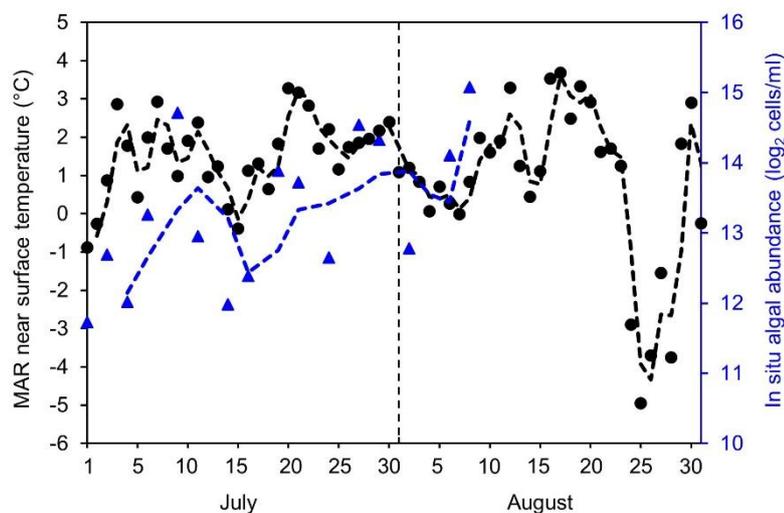
515 **Figure B1. MAR-simulated near surface temperature (°C, black circle, left axis) and in situ measured algal abundance (log2 cells/ml, blue triangle, right vertical axis) over the S6 weather station at K-transect during 2014 July-August by Stibal et al. (2017).**

Author contribution

S.W., M.T., and P.A. designed the study. S.W. processed the MERIS, MODIS, and WorldView-2 data. S.W. and M.X. tested the MERIS ratio indices. X.F. provided the MAR v3.9 outputs. S.W., M.T., and P.A. analysed the results and generated figures.

520 S. W. wrote the manuscript. All authors discussed the results and contributed to the final manuscript.

Competing interests

The authors declare that they have no conflict of interest.

Acknowledgement

This work was supported by National Science Foundation ANS #1713072, National Science Foundation PLR-1603331, NASA
525 Exobiology award #80NSSC18K0814, NASA MAP #80NSSC17K0351, NASA #NNX17AH04G, and the Heising-Simons foundation. We would like to thank the Polar Geospatial Center (https://www.pgc.umn.edu/) for providing the WorldView-2 imagery, the European Space Agency for distributing the MERIS data, and the NASA Land Processes Distributed Active Archive Center for distributing the MODIS data. Thanks to David Porter (Lamont-Doherty Earth Observatory, Columbia University) and Rafael Antwerpen (Utrecht University) for commenting on the final manuscript.

530 **References**

Alexander, P. M., Tedesco, M., Fettweis, X., van de Wal, R. S. W., Smeets, C. J. P. P. and van den Broeke, M. R.: Assessing spatio-temporal variability and trends in modelled and measured Greenland Ice Sheet albedo (2000–2013), The Cryosphere, 8(6), 2293–2312, 2014.

Anderson, G. P., Felde, G. W., Hoke, M. L., Ratkowski, A. J., Cooley, T. W., Chetwynd, J. H., Gardner, J. A., Adler-Golden,
535 S. M., Matthew, M. W., Berk, A., Bernstein, L. S., Acharya, P. K., Miller, D. P. and Lewis, P. E.: MODTRAN4-based atmospheric correction algorithm: FLAASH (fast line-of-sight atmospheric analysis of spectral hypercubes), in Algorithms and Technologies for Multispectral, Hyperspectral, and Ultraspectral Imagery VIII, vol. 4725, pp. 65–72, International Society for Optics and Photonics., 2002.

Anesio, A. M., Lutz, S., Chrismas, N. A. M. and Benning, L. G.: The microbiome of glaciers and ice sheets, NPJ Biofilms
540 Microbiomes, 3, 10, 2017.

Beck, R., Zhan, S., Liu, H., Tong, S., Yang, B., Xu, M., Ye, Z., Huang, Y., Shu, S., Wu, Q., Wang, S., Berling, K., Murray, A., Emery, E., Reif, M., Harwood, J., Young, J., Nietch, C., Macke, D., Martin, M., Stillings, G., Stump, R. and Su, H.: Comparison of satellite reflectance algorithms for estimating chlorophyll-a in a temperate reservoir using coincident hyperspectral aircraft imagery and dense coincident surface observations, Remote Sens. Environ., 178(Supplement C), 15–30,
545 2016.

Binding, C. E., Greenberg, T. A. and Bukata, R. P.: The MERIS Maximum Chlorophyll Index; its merits and limitations for inland water algal bloom monitoring, J. Great Lakes Res., 39, 100–107, 2013.

Blondeau-Patissier, D., Gower, J. F. R., Dekker, A. G., Phinn, S. R. and Brando, V. E.: A review of ocean color remote sensing methods and statistical techniques for the detection, mapping and analysis of phytoplankton blooms in coastal and open oceans,
550 Prog. Oceanogr., 123, 123–144, 2014.

Box, J. E., Cappelen, J., Decker, D., Fettweis, X., Mote, T., Tedesco, M. and van de Wal, R. S. W. Greenland [in Arctic Report Card 2010]. Retrieved from https://arctic.noaa.gov/Report-Card/Report-Card-Archive, 2010.

Box, J. E., Fettweis, X., Stroeve, J. C., Tedesco, M., Hall, D. K. and Steffen, K.: Greenland ice sheet albedo feedback: thermodynamics and atmospheric drivers, The Cryosphere, 6(4), 821–839, 2012.

555 Casey, K. A., Polashenski, C. M., Chen, J. and Tedesco, M.: Impact of MODIS sensor calibration updates on Greenland Ice Sheet surface reflectance and albedo trends, The Cryosphere, 11(4), 1781–1795, 2017.

Cavicchioli, R., Ripple, W. J., Timmis, K. N., Azam, F., Bakken, L. R., Baylis, M., Behrenfeld, M. J., Boetius, A., Boyd, P. W., Classen, A. T., Crowther, T. W., Danovaro, R., Foreman, C. M., Huisman, J., Hutchins, D. A., Jansson, J. K., Karl, D. M., Koskella, B., Mark Welch, D. B., Martiny, J. B. H., Moran, M. A., Orphan, V. J., Reay, D. S., Remais, J. V., Rich, V. I., Singh,
560 B. K., Stein, L. Y., Stewart, F. J., Sullivan, M. B., van Oppen, M. J. H., Weaver, S. C., Webb, E. A. and Webster, N. S.: Scientists' warning to humanity: microorganisms and climate change, Nat. Rev. Microbiol., doi:10.1038/s41579-019-0222-5, 2019.

Chandler, D. M., Alcock, J. D., Wadham, J. L., Mackie, S. L. and Telling, J.: Seasonal changes of ice surface characteristics and productivity in the ablation zone of the Greenland Ice Sheet, The Cryosphere, 9(2), 487–504, 2015.

565 Cook, J. M., Tedstone, A. J., Williamson, C., McCutcheon, J., Hodson, A. J., Dayal, A., Skiles, M., Hofer, S., Bryant, R., McAree, O., McGonigle, A., Ryan, J., Anesio, A. M., Irvine-Fynn, T. D. L., Hubbard, A., Hanna, E., Flanner, M., Mayanna, S., Benning, L. G., van As, D., Yallop, M., McQuaid, J., Gribbin, T. and Tranter, M.: Glacier algae accelerate melt rates on the western Greenland Ice Sheet, The Cryosphere, doi:10.5194/tc-2019-58, 2019.

Dee, D. P., Uppala, S. M., Simmons, A. J., Berrisford, P., Poli, P., Kobayashi, S., Andrae, U., Balmaseda, M. A., Balsamo,
570 G., Bauer, P., Bechtold, P., Beljaars, A. C. M., van de Berg, L., Bidlot, J., Bormann, N., Delsol, C., Dragani, R., Fuentes, M., Geer, A. J., Haimberger, L., Healy, S. B., Hersbach, H., Hólm, E. V., Isaksen, L., Kållberg, P., Köhler, M., Matricardi, M., McNally, A. P., Monge-Sanz, B. M., Morcrette, J.-J., Park, B.-K., Peubey, C., de Rosnay, P., Tavolato, C., Thépaut, J.-N., and Vitart, F.: The ERA-Interim reanalysis: configuration and performance of the data assimilation system, Q. J. Roy. Meteorol. Soc., 137, 553–597, doi:10.1002/qj.828, 2011.

575 De Ridder, K. and Gallée, H.: Land Surface–Induced Regional Climate Change in Southern Israel, J. Appl. Meteorol., 37(11), 1470–1485, 1998.

Di Mauro, B., Fava, F., Ferrero, L., Garzonio, R., Baccolo, G., Delmonte, B. and Colombo, R.: Mineral dust impact on snow radiative properties in the European Alps combining ground, UAV, and satellite observations, J. Geophys. Res. D: Atmos., 120(12), 6080–6097, 2015.

580 Dumont, M., Brun, E., Picard, G., Michou, M., Libois, Q., Petit, J.-R., Geyer, M., Morin, S. and Josse, B.: Contribution of light-absorbing impurities in snow to Greenland's darkening since 2009, Nat. Geosci., 7, 509, 2014.

European Space Agency (ESA): MERIS Product Handbook, Issue 3.0, 1 August 2011.

European Space Agency (ESA): MERIS Algorithm Theoretical Basis Document 2-17-Pixel Classification, Issue 5.0, 30 May 2011.

585 Fettweis, X., Tedesco, M., van den Broeke, M. and Ettema, J.: Melting trends over the Greenland ice sheet (1958–2009) from spaceborne microwave data and regional climate models, The Cryosphere, 5(2), 359–375, doi:10.5194/tc-5-359-2011, 2011.

Fettweis, X., Box, J., Agosta, C., Amory, C., Kittel, C., Lang, C., van As, D., Machguth, H. and Gallée, H.: Reconstructions of the 1900--2015 Greenland ice sheet surface mass balance using the regional climate MAR model, Cryosphere (The), 11, 1015–1033, 2017.

590 Flanner, M. G., Zender, C. S., Randerson, J. T. and Rasch, P. J.: Present-day climate forcing and response from black carbon in snow, J. Geophys. Res., 112(D11), 3131, 2007.

Gallée, H. and Schayes, G.: Development of a Three-Dimensional Meso-γ Primitive Equation Model: Katabatic Winds Simulation in the Area of Terra Nova Bay, Antarctica, Mon. Weather Rev., 122(4), 671–685, 1994.

Ganey, G. Q., Loso, M. G., Burgess, A. B. and Dial, R. J.: The role of microbes in snowmelt and radiative forcing on an
595 Alaskan icefield, Nat. Geosci., 10, 754, 2017.

Gitelson, A.: The peak near 700 nm on radiance spectra of algae and water: relationships of its magnitude and position with chlorophyll concentration, Int. J. Remote Sens., 13(17), 3367–3373, 1992.

Goelles, T. and Bøggild, C. E.: Albedo reduction of ice caused by dust and black carbon accumulation: a model applied to the K-transect, West Greenland, J. Glaciol., 63(242), 1063–1076, 2017.

600 Gower, J., King, S. and Goncalves, P.: Global monitoring of plankton blooms using MERIS MCI, Int. J. Remote Sens., 29(21), 6209–6216, 2008.

Hall, D. K. and Martinec, J.: Remote sensing of snow and ice, Principles and Applications of Imaging Radar, edited by FM Henderson and AJ Lewis, 677–703, 1985.

Hanna, E., Cropper, T. E., Hall, R. J. and Cappelen, J.: Greenland Blocking Index 1851-2015: a regional climate change signal, 605 Int. J. Climatol., 36(15), 4847–4861, 2016.

Hofer, S., Tedstone, A. J., Fettweis, X. and Bamber, J. L.: Decreasing cloud cover drives the recent mass loss on the Greenland Ice Sheet, Sci Adv, 3(6), e1700584, 2017.

Howat, I. M., Negrete, A. and Smith, B. E.: The Greenland Ice Mapping Project (GIMP) land classification and surface elevation data sets, The Cryosphere, 8(4), 1509–1518, 2014.

610 Huovinen, P., Ramírez, J. and Gómez, I.: Remote sensing of albedo-reducing snow algae and impurities in the Maritime Antarctica, ISPRS J. Photogramm. Remote Sens., 146, 507–517, 2018.

Legleiter, C. J., Tedesco, M., Smith, L. C. and Overstreet, B. T.: Mapping the bathymetry of supraglacial lakes and streams on the Greenland Ice Sheet using field measurements and high resolution satellite images, The Cryosphere Discussions, 7(5), 4741–4773, doi:10.5194/tcd-7-4741-2013, 2013.

615 Lutz, S., Anesio, A. M., Jorge Villar, S. E. and Benning, L. G.: Variations of algal communities cause darkening of a Greenland glacier, FEMS Microbiol. Ecol., 89(2), 402–414, 2014.

Lutz, S., Anesio, A. M., Raiswell, R., Edwards, A., Newton, R. J., Gill, F. and Benning, L. G.: The biogeography of red snow microbiomes and their role in melting arctic glaciers, Nat. Commun., 7, 11968, 2016.

Lutz, S., Anesio, A. M., Edwards, A. and Benning, L. G.: Linking microbial diversity and functionality of arctic glacial surface 620 habitats, Environ. Microbiol., 19(2), 551–565, 2017.

Lutz, S., McCutcheon, J., McQuaid, J. B. and Benning, L. G.: The diversity of ice algal communities on the Greenland Ice Sheet as revealed by oligotyping, Microb Genom, doi:10.1099/mgen.0.000159, 2018.

Lyapustin, A., Tucker, J., Hall, F., Sellers, P., Wu, A., Angal, A., Wang, Y., Xiong, X., Meister, G., Platnick, S. and Others: Scientific impact of MODIS C5 calibration degradation and C6+ improvements, Atmospheric Measurement Techniques, 7(12) 625 [online] Available from: https://ir.library.oregonstate.edu/concern/articles/b2773x521, 2014.

Matthews, M. W.: A current review of empirical procedures of remote sensing in inland and near-coastal transitional waters, Int. J. Remote Sens., 32(21), 6855–6899, 2011.

Mioduszewski, J. R., Rennermalm, A. K., Hammann, A., Tedesco, M., Noble, E. U., Stroeve, J. C. and Mote, T. L.: Atmospheric drivers of Greenland surface melt revealed by self-organizing maps, J. Geophys. Res. D: Atmos., 121(10), 2015JD024550, 2016.

Mishra, S. and Mishra, D. R.: Normalized difference chlorophyll index: A novel model for remote estimation of chlorophyll-a concentration in turbid productive waters, Remote Sens. Environ., 117, 394–406, 2012.

Moses, W. J., Gitelson, A. A., Berdnikov, S. and Povazhnyy, V.: Satellite Estimation of Chlorophyll-a Concentration Using the Red and NIR Bands of MERIS—The Azov Sea Case Study, IEEE Geoscience and Remote Sensing Letters, 6(4), 845–849, doi:10.1109/lgrs.2009.2026657, 2009.

Moses, W. J., Gitelson, A. A., Berdnikov, S., Saprygin, V. and Povazhnyi, V.: Operational MERIS-based NIR-red algorithms for estimating chlorophyll-a concentrations in coastal waters—The Azov Sea case study, Remote Sens. Environ., 121, 118–124, 2012.

Moustafa, S. E., Rennermalm, A. K., Smith, L. C., Miller, M. A., Mioduszewski, J. R., Koenig, L. S., Hom, M. G. and Shuman, C. A.: Multi-modal albedo distributions in the ablation area of the southwestern Greenland Ice Sheet, The Cryosphere, 9(3), 905–923, 2015.

Nordenskiöld, A. E.: I.—Account of an Expedition to Greenland in the year 1870, Geol. Mag., 9(97), 289–306, 1872.

Painter, T. H., Duval, B., Thomas, W. H., Mendez, M., Heintzelman, S. and Dozier, J.: Detection and quantification of snow algae with an airborne imaging spectrometer, Appl. Environ. Microbiol., 67(11), 5267–5272, 2001.

Palmer, S. C. J., Hunter, P. D., Lankester, T., Hubbard, S., Spyrakos, E., N. Tyler, A., Présing, M., Horváth, H., Lamb, A., Balzter, H. and Tóth, V. R.: Validation of Envisat MERIS algorithms for chlorophyll retrieval in a large, turbid and optically-complex shallow lake, Remote Sens. Environ., 157, 158–169, 2015.

Remias, D., Schwaiger, S., Aigner, S., Leya, T., Stuppner, H. and Lütz, C.: Characterization of an UV-and VIS-absorbing, purpurogallin-derived secondary pigment new to algae and highly abundant in M esotaenium berggrenii (Z ygnematophyceae, Chlorophyta), an extremophyte living on glaciers, FEMS Microbiol. Ecol., 79(3), 638–648, 2012.

Reshitnyk, L., Costa, M., Robinson, C. and Dearden, P.: Evaluation of WorldView-2 and acoustic remote sensing for mapping benthic habitats in temperate coastal Pacific waters, Remote Sens. Environ., 153, 7–23, 2014.

Ryan, J. C., Hubbard, A., Stibal, M., Irvine-Fynn, T. D., Cook, J., Smith, L. C., Cameron, K. and Box, J.: Dark zone of the Greenland Ice Sheet controlled by distributed biologically-active impurities, Nat. Commun., 9(1), 1065, 2018.

Shimada, R., Takeuchi, N. and Aoki, T.: Inter-Annual and Geographical Variations in the Extent of Bare Ice and Dark Ice on the Greenland Ice Sheet Derived from MODIS Satellite Images, Front. Earth Sci., 4, 2293, 2016.

Skiles, S. M., Flanner, M., Cook, J. M., Dumont, M. and Painter, T. H.: Radiative forcing by light-absorbing particles in snow, Nat. Clim. Chang., 8(11), 964–971, 2018.

Stibal, M., Gözdereliler, E., Cameron, K. A., Box, J. E., Stevens, I. T., Gokul, J. K., Schostag, M., Zarsky, J. D., Edwards, A., Irvine-Fynn, T. D. L. and Jacobsen, C. S.: Microbial abundance in surface ice on the Greenland Ice Sheet, Front. Microbiol., 6, 225, 2015.

Stibal, M., Box, J. E., Cameron, K. A., Langen, P. L., Yallop, M. L., Mottram, R. H., Khan, A. L., Molotch, N. P., Chrismas, N. A. M., Calì Quaglia, F., Remias, D., Smeets, C. J. P. P., van den Broeke, M. R., Ryan, J. C., Hubbard, A., Tranter, M., van As, D. and Ahlstrøm, A. P.: Algae Drive Enhanced Darkening of Bare Ice on the Greenland Ice Sheet, Geophys. Res. Lett., 44(22), 2017GL075958, 2017.

Stroeve, J., Box, J. E., Wang, Z., Schaaf, C. and Barrett, A.: Re-evaluation of MODIS MCD43 Greenland albedo accuracy and trends, Remote Sens. Environ., 138, 199–214, 2013.

Takeuchi, N.: The altitudinal distribution of snow algae on an Alaska glacier (Gulkana Glacier in the Alaska Range), Hydrol. Process., 15(18), 3447–3459, 2001.

Takeuchi, N., Dial, R., Kohshima, S., Segawa, T. and Uetake, J.: Spatial distribution and abundance of red snow algae on the Harding Icefield, Alaska derived from a satellite image, Geophys. Res. Lett., 33(21), 570, 2006.

Takeuchi, N., Nagatsuka, N., Uetake, J. and Shimada, R.: Spatial variations in impurities (cryoconite) on glaciers in northwest Greenland, Bull. Glaciol. Res., 32, 85–94, 2014.

Tedesco, M., Fettweis, X., van den Broeke, M. R., van de Wal, R. S. W., C J P, van de Berg, W. J., Serreze, M. C. and Box, J. E.: The role of albedo and accumulation in the 2010 melting record in Greenland, Environ. Res. Lett., 6(1), 014005, 2011.

Tedesco, M., Doherty, S., Fettweis, X., Alexander, P., Jeyaratnam, J. and Stroeve, J.: The darkening of the Greenland ice sheet: trends, drivers, and projections (1981–2100), The Cryosphere, 10(2), 477–496, 2016.

Tedesco, M., Box, J. E., Cappelen, J., Fausto, R. S., Fettweis, X., Andersen, J. K., Mote, T., Smeets, C. J. P. P., van As, D. and van de Wal, R. S. W.: Greenland Ice Sheet [in Arctic Report Card 2018]. Retrieved from https://arctic.noaa.gov/Report-Card/Report-Card-2018/ArtMID/7878/ArticleID/781/Greenland-Ice-Sheet, 2018.

Tedstone, A. J., Bamber, J. L., Cook, J. M., Williamson, C. J., Fettweis, X., Hodson, A. J. and Tranter, M.: Dark ice dynamics of the south-west Greenland Ice Sheet, The Cryosphere, 11(6), 2491–2506, 2017.

Toller, G., Xiong, X. J., Sun, J., Wenny, B. N., Geng, X., Kuyper, J., Angal, A., Chen, H., Madhavan, S. and Wu, A.: Terra and Aqua moderate-resolution imaging spectroradiometer collection 6 level 1B algorithm, JARS, 7(1), 073557, 2013.

Uetake, J., Naganuma, T., Hebsgaard, M. B., Kanda, H. and Kohshima, S.: Communities of algae and cyanobacteria on glaciers in west Greenland, Polar Sci., 4(1), 71–80, 2010.

Wang, S., Liu, H., Yu, B., Zhou, G. and Cheng, X.: Revealing the early ice flow patterns with historical Declassified Intelligence Satellite Photographs back to 1960s, Geophys. Res. Lett., 43(11), 2016GL068990, 2016.

Wang, S., Tedesco, M., Xu, M. and Alexander, P. M.: Mapping Ice Algal Blooms in Southwest Greenland From Space, Geophys. Res. Lett., 45(21), 11,779–11,788, 2018.

Warren, S. G.: Optical properties of snow, Rev. Geophys., 20(1), 67, 1982.

Wientjes, I. G. M. and Oerlemans, J.: An explanation for the dark region in the western melt zone of the Greenland ice sheet, The Cryosphere, 4(3), 261–268, 2010.

Wientjes, I. G. M., Wal, R. S. W. V. de, Reichart, G. J., Sluijs, A. and Oerlemans, J.: Dust from the dark region in the western ablation zone of the Greenland ice sheet, The Cryosphere, 5(3), 589–601, 2011.

Wientjes, I. G. M., Van De Wal, R. S. W., Schwikowski, M., Zapf, A., Fahrni, S. and Wacker, L.: Carbonaceous particles reveal that Late Holocene dust causes the dark region in the western ablation zone of the Greenland ice sheet, J. Glaciol., 58(210), 787–794, 2012.

Williamson, C. J., Anesio, A. M., Cook, J., Tedstone, A., Poniecka, E., Holland, A., Fagan, D., Tranter, M. and Yallop, M. L.: Ice algal bloom development on the surface of the Greenland Ice Sheet, FEMS Microbiol. Ecol., 94(3), doi:10.1093/femsec/fiy025, 2018.

Williamson, C. J., Cameron, K. A., Cook, J. M., Zarsky, J. D., Stibal, M. and Edwards, A.: Glacier Algae: A Dark Past and a Darker Future, Front. Microbiol., 10, 524, 2019.

Xu, M., Liu, H., Beck, R., Lekki, J., Yang, B., Shu, S., Kang, E. L., Anderson, R., Johansen, R., Emery, E., Reif, M. and Benko, T.: A spectral space partition guided ensemble method for retrieving chlorophyll-a concentration in inland waters from Sentinel-2A satellite imagery, Journal of Great Lakes Research, 45(3), 454–465, doi:10.1016/j.jglr.2018.09.002, 2019a.

Xu, M., Liu, H., Beck, R., Lekki, J., Yang, B., Shu, S., Liu, Y., Benko, T., Anderson, R., Tokars, R., Johansen, R., Emery, E. and Reif, M.: Regionally and Locally Adaptive Models for Retrieving Chlorophyll-a Concentration in Inland Waters From Remotely Sensed Multispectral and Hyperspectral Imagery, IEEE Transactions on Geoscience and Remote Sensing, 57(7), 4758–4774, doi:10.1109/tgrs.2019.2892899, 2019b.

Yallop, M. L., Anesio, A. M., Perkins, R. G., Cook, J., Telling, J., Fagan, D., MacFarlane, J., Stibal, M., Barker, G., Bellas, C., Hodson, A., Tranter, M., Wadham, J. and Roberts, N. W.: Photophysiology and albedo-changing potential of the ice algal community on the surface of the Greenland ice sheet, ISME J., 6(12), 2302–2313, 2012.

Yang, K. and Smith, L. C.: Supraglacial streams on the Greenland Ice Sheet delineated from combined spectral--shape information in high-resolution satellite imagery, IEEE Geoscience and Remote Sensing Letters, 10(4), 801–805, 2013.